# Disease-associated mutations in inositol 1,4,5-trisphosphate receptor subunits impair channel function

Received for publication, August 17, 2020, and in revised form, October 21, 2020 Published, Papers in Press, October 22, 2020, DOI 10.1074/jbc.RA120.015683

**Lara E. Terry, Kamil J. Alzayady, Amanda M. Wahl, Sundeep Malik, and David I. Yule***

*From the Department of Pharmacology and Physiology, University of Rochester, Rochester, New York, USA*

Edited by Roger J. Colbran

**The inositol 1,4,5-trisphosphate ($IP_3$) receptors ($IP_3Rs$), which form tetrameric channels, play pivotal roles in regulating the spatiotemporal patterns of intracellular calcium signals. Mutations in $IP_3Rs$ have been increasingly associated with many debilitating human diseases such as ataxia, Gillespie syndrome, and generalized anhidrosis. However, how these mutations affect $IP_3R$ function, and how the perturbation of associated calcium signals contribute to the pathogenesis and severity of these diseases remains largely uncharacterized. Moreover, many of these diseases occur as the result of autosomal dominant inheritance, suggesting that WT and mutant subunits associate in heterotetrameric channels. How the incorporation of different numbers of mutant subunits within the tetrameric channels affects its activities and results in different disease phenotypes is also unclear. In this report, we investigated representative disease-associated missense mutations to determine their effects on $IP_3R$ channel activity. Additionally, we designed concatenated $IP_3R$ constructs to create tetrameric channels with a predefined subunit composition to explore the functionality of heteromeric channels. Using calcium imaging techniques to assess $IP_3R$ channel function, we observed that all the mutations studied resulted in severely attenuated $Ca^{2+}$ release when expressed as homotetramers. However, some heterotetramers retained varied degrees of function dependent on the composition of the tetramer. Our findings suggest that the effect of mutations depends on the location of the mutation in the $IP_3R$ structure, as well as on the stoichiometry of mutant subunits assembled within the tetrameric channel. These studies provide insight into the pathogenesis and penetrance of these devastating human diseases.**

Inositol 1,4,5-trisphosphate ($IP_3$) receptor ($IP_3R$)-mediated calcium ($Ca^{2+}$) release regulates many cellular activities including proliferation, secretion, division, contraction, and even apoptosis (1–11). There are three $IP_3R$ genes in the human genome (*ITPR1, ITPR2,* and *ITPR3*). The resulting monomeric isoforms of $IP_3R$ ($IP_3R1$, $IP_3R2$, and $IP_3R3$) share ~60–70% sequence homology and form homo- and heterotetrameric $Ca^{2+}$ channels predominantly located in membranes of intracellular $Ca^{2+}$ stores (3, 12–18). In response to various extracellular stimuli that induce phospholipase C-mediated hydrolysis of phosphatidylinositol 4,5-bisphosphate, $IP_3$ is generated and diffuses through the cytosol to bind and subsequently activate $IP_3R$ channels resulting in movement of $Ca^{2+}$ down its concentration gradient into the cytosol (19, 20). Each monomeric $IP_3R$ isoform is a ~300 kDa protein and is generally divided into four functional domains (Fig. 1). The N-terminal suppressor domain (SD; 1-225 aa)[1] (21) and ligand-binding domain (LBD; 226-578 aa) (22), the central regulatory and coupling domain (579-2232 aa) (23), and the C-terminal channel domain containing six membrane spanning regions and a cytosolic tail (2233-2710 aa) (24–26). It is believed that $IP_3$ binding to the N terminus of $IP_3R$ triggers conformational changes that are transmitted intramolecularly or intermolecularly to open the channel pore located at the C terminus (27–30); however, the precise mechanism of this gating is uncertain (31).

$IP_3R$ genes are ubiquitously expressed, although various tissues and cell types often preferentially express one subtype or a combination of subtypes (32–35). Despite the overlapping expression patterns, these receptors can mediate distinct functions depending on the cell's physiological context. $IP_3R1$ is highly enriched in the nervous system, whereas $IP_3R2$ and $IP_3R3$ are predominately expressed in the periphery including the digestive system and secretory cells of the exocrine system (36–38). Studies have shown that $IP_3R1$ is essential for normal nervous system development as mice lacking $IP_3R1$ often die *in utero* or suffer from severe ataxia and seizure prior to death very early in postnatal life (39–41). Mice lacking either $IP_3R2$ or $IP_3R3$ appear to develop only subtle phenotypes. However, mice lacking both $IP_3R2$ and $IP_3R3$ suffer from severe salivary and pancreatic insufficiencies and die after weaning due to inability to assimilate macronutrients from dry food (42).

Many devastating human diseases have been associated with abnormal $Ca^{2+}$ homeostasis. Indeed, there is a growing body of literature illustrating that diseases, such as Huntington's disease, schizophrenia, ALS, Parkinson's disease, Alzheimer's disease, and spinocerebellar ataxia (SCA), are all accompanied by dysregulated $Ca^{2+}$ signals (43–46). Although the underlying etiologies of these diseases are heterogeneous, many studies have shown that perturbed $IP_3R$ signaling is among the contributing or causal factors. Mutations in $IP_3R$ genes have been associated with several human diseases, including SCA (47–53), Gillespie syndrome (GS) (52, 54), and anhidrosis (55). These mutations have generally been identified through whole exome

This article contains supporting information.

* For correspondence: David I. Yule, David_Yule@urmc.rochester.edu.
Present address for Kamil J. Alzayady: Physician Assistant Department, University of Maryland Eastern Shore, Princess Anne, Maryland, USA

[1] The nucleotide sequences, and thus amino acid numbering, used throughout this paper are: $rIP_3R1$, NM_001007235; $hIP_3R1$, NM_001099952; $mIP_3R2$, NM_019923. See Table S6 for alignment guide of these sequences with other commonly used sequences.

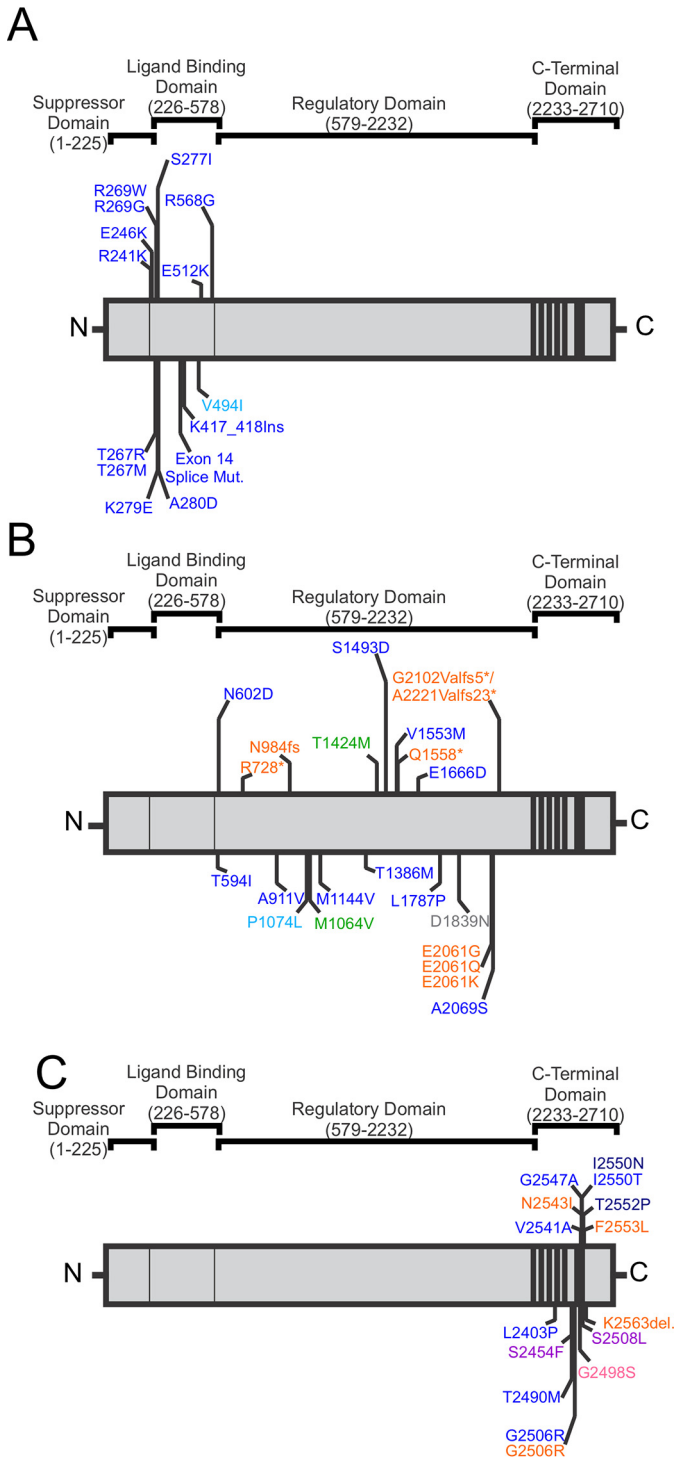


**Figure 1. Linear schematic of the four domains of the IP$_3$R and the disease-associated IP$_3$R mutations found in the LBD, regulatory and coupling, and C-terminal domains.** *A,* disease-associated mutations found in the LBD (49–53, 68–71). *B*, disease-associated mutations found in the regulatory and coupling domain (47–49, 52–54, 65, 72–82). *C,* disease-associated mutations found in the C-terminal domain (52–55, 65, 83–89). Diseases associated with mutations in at least one isoform of IP$_3$R include SCA29 (*blue*), Gillespie syndrome (*orange*), anhidrosis (*pink*), neuropathy (*green*), pontocerebellar hypoplasia (*dark blue*), spinocerebellar ataxia 15/16 (*light blue*), head and neck squamous cell carcinoma (*red*), Sézary Syndrome (*purple*), and familial isolated primary hyperparathyroidism (*gray*).

sequencing and linkage analysis in a clinical setting. Nevertheless, the molecular and cellular consequences of many of these mutations, as well as the mechanism whereby individual mutations lead to the clinical manifestations, remain largely unknown. As mutations have been identified in all four functional domains of the IP$_3$R, it is conceivable that mutations can interfere with various aspects of IP$_3$R biology including IP$_3$ binding, allosteric regulation by various cellular factors, ion permeation, protein folding, stability, and subcellular localization. It is likely that in patients, tetrameric IP$_3$R channels are assembled from a combination of both WT and mutant subunits and given the autosomal dominant inheritance of the majority of cases, the incorporation of mutant subunits likely results in dominant-negative activity. Nevertheless, how the specific stoichiometry of the resultant heterotetrameric channels might affect function and lead to different clinical manifestations and disease penetrance have not been explored.

In this study, we have examined the consequences of a representative set of missense mutations on IP$_3$R channel function that are illustrative of mutations in distinct functional domains of the IP$_3$R and of differing modes of inheritance. Missense mutations of residues Arg-269 (R269W) (50–53) and Asn-602 (N602D) (47, 48, 52) both lead to multiple cases of autosomal dominant, early-onset, nonprogressive ataxia, even though they are located in the LBD and regulatory/coupling domain, respectively (Fig. 1, *A* and *B*). In contrast, the G2498S mutation, located in the C-terminal selectivity filter of the IP$_3$R2 channel pore (Fig. 1*C*), is inherited in an autosomal recessive fashion such that individuals homozygous for the mutation suffered from generalized anhidrosis, whereas their family members heterozygous for the mutation were asymptomatic for the disease (55). We utilized two heterologous expression systems, which are unambiguously IP$_3$R *null* (56, 57) to directly investigate how expression of these mutant channels affect channel expression and localization, tetramer formation, IP$_3$ binding, channel gating, $Ca^{2+}$ store content, and $Ca^{2+}$ release activities. To investigate how incorporation of WT and disease-associated mutant subunits into the assembled receptor alters channel function, we also used a concatenated subunit approach that allows for a defined subunit stoichiometry. Our data indicate that the impact of missense mutations is domain dependent and markedly impacted by the stoichiometry of incorporation into the functional heterotetrameric channel. These studies provide a framework to understand the molecular basis of human IP$_3$R pathologies and offer novel insight into roles of key residues in IP$_3$R channel activities.

## Results

IP$_3$R1 is highly expressed in the nervous system (35) and mutations result in a broad range of disease phenotypes: ataxia alone or ataxia with cognitive difficulties, iris hypoplasia and/or cerebellar hypotrophy. Indeed, there is a growing list of missense (47–55), nonsense, insertion/deletion, and splice mutations (58, 59) scattered throughout the IP$_3$R1 gene (Fig. 1). Nevertheless,

how $IP_3R1$ mutations affect channel activity and how these mutations lead to pathogenesis remains to be elucidated. Here we investigated in detail, the functional consequences of three representative mutations located in different functional domains of $IP_3R$ following expression of homotetrameric or defined heterotetrameric mutant channels in an $IP_3R$ *null* background.

### *Mutation of R269W attenuates $IP_3R$ activity by reducing $IP_3$ binding*

R269W has been identified in patients diagnosed with autosomal dominant, nonprogressive congenital ataxia (NPCA) (50), spinocerebellar ataxia 29 (SCA29) (52), ataxic cerebral palsy (51), and early-onset ataxia (EOA) (53). These patients exhibit nonprogressive early-onset ataxia, hypotonia, and developmental delays (Table S1). Residue Arg-269 is located in the ligand-binding core of the $IP_3R1$ (Table S2) that also constitutes the $IP_3R$-binding protein released with inositol 1,4,5-trisphosphate (IRBIT)-binding domain (60, 61). This mutation (R269W) substitutes an evolutionarily conserved (Fig. 2*A*), positively charged, arginine residue, with a large hydrophobic, aromatic, tryptophan residue (Fig. 2*B*). This residue has been previously identified as one of the 12 positively charged amino acids absolutely required for $IP_3$ binding and early studies have demonstrated that mutation of arginine to glutamine at this site (R269Q) resulted in an 80% loss of $IP_3$ binding (22, 62). We therefore investigated the consequences of the R269W mutation on $IP_3$ binding. WT, rat $IP_3R1$ (WT $rIP_3R1$), and rat cDNA engineered to express the R269W mutation ($rIP_3R1^{RW}$) were stably transfected into DT40-3KO cells (56) (Fig. 2*C*). [$^3$H]$IP_3$ binding was measured by competitive binding assays. When exogenously expressed in DT40-3KO, $rIP_3R1^{RW}$ $IP_3$-binding activity was severely compromised compared with WT $rIP_3R1$ (Fig. 2*D*). Total specific binding was reduced by 60%, whereas the apparent $EC_{50}$ for binding was not markedly altered under these conditions. This latter observation is surprising but may reflect severe alterations in the binding kinetics (either an alteration of on- or off-rate) such that equilibrium binding is not reached for the $rIP_3R1^{RW}$ mutant under the same conditions as the WT $rIP_3R1$.

Next, we assessed the ability of $rIP_3R1^{RW}$ to support $IP_3$-induced $Ca^{2+}$ release when stably expressed in DT40-3KO cells. In single cell imaging experiments, stimulation with trypsin, which activates the $G\alpha_q$-coupled protease-activated receptor 2 (PAR2), generates $IP_3$ and results in $Ca^{2+}$ release in cells expressing $rIP_3R1$ but not in $IP_3R$ *null*, DT40-3KO (Fig. 2*E*) (56, 57). Similarly, whereas stimulation of cells expressing $rIP_3R1$ receptors mediated robust $Ca^{2+}$ signals, cells expressing $rIP_3R1^{RW}$ did not exhibit any measurable response to a maximal concentration of trypsin (Fig. 2*E*). The pooled data illustrates that despite retaining modest residual binding activity, in terms of the magnitude of signal (Fig. 2*F*), and the number of cells that respond above a defined threshold (Fig. 2*G*), $rIP_3R1^{RW}$ is refractory to stimulation in DT40-3KO cells. Additionally, multiple, distinct clonal $rIP_3R1^{RW}$ cell lines generated in DT40-3KO cells exhibited similar decreases in amplitude (data not shown). This lack of response may be related to the requirement of each $IP_3R$ monomer to be occupied by $IP_3$ for activation (57), which given the reduced binding, would be predicted to limit this occurrence.

In support of the idea that assemblies of mutant (binding deficient) $IP_3R1$ and WT $IP_3R1$ are generated in cells, we performed co-immunoprecipitation experiments in cells transfected with a mCherry-tagged $rIP_3R1$ and $IP_3R1^{RW}$. The $IP_3R1^{RW}$ mutant was readily detected in samples immunoprecipitated with a mCherry antibody (Fig. S1*A*) and thus heterotetrameric channels containing both WT and mutant subunits were formed.

A prediction from our previous data (57) is that heterotetramers consisting of $rIP_3R1$ and $rIP_3R1^{RW}$ would also fail to respond to stimulation. To test this idea, we generated cDNA encoding concatenated dimers consisting of $rIP_3R1$ and $rIP_3R1^{RW}$ expressed as a single polypeptide chain of $IP_3R1$-$IP_3R1^{RW}$ ($R1/R1^{RW}$) or $IP_3R1^{RW}$-$IP_3R1$ ($R1^{RW}/R1$) and stably expressed these constructs in DT40-3KO cells (Fig. 3*A*). Dimers are assembled by the cell to produce tetrameric channels consisting of two $IP_3R1$ and two $IP_3R1^{RW}$ subunits. Cells expressing concatenated dimers encoding only $rIP_3R1$ (R1/R1) responded to PAR2 stimulation with robust $Ca^{2+}$ signals, as previously reported (38, 57), whereas cells expressing concatenated dimers encoding $rIP_3R1^{RW}$ ($R1^{RW}/R1^{RW}$) failed to respond (Fig. 3*B*). Additionally, cells expressing $R1/R1^{RW}$ or $R1^{RW}/R1$ dimers also failed to respond to trypsin stimulation (Fig. 3*B*). The pooled data illustrates that despite some $R1/R1^{RW}$ or $R1^{RW}/R1$ dimers exhibiting a very small increase in the magnitude of the signal (Fig. 3*C*), the number of cells that respond above to a defined threshold remained not significantly different from the null DT40-3KO cell line (Fig. 3*D*). Additional $R1/R1^{RW}$, $R1^{RW}/R1$, and $R1^{RW}/R1^{RW}$ dimeric clonal cell lines generated in DT40-3KO cells exhibited similar decreases in amplitude and percentage of cells responding above a specific threshold (data not shown). Consistent with these observations, $IP_3$ also failed to evoke $Ca^{2+}$ release in permeabilized DT40-3KO cells stably expressing channels containing two or more $rIP_3R1^{RW}$ subunits (Fig. 3*E*). These data indicate that tetramers containing mutant subunits likely are poorly functional. Thus, the implication is that patients with heterozygous expression of the mutant protein, only tetramers consisting of nonmutant $IP_3R1$ subunits would support significant function.

Although the DT40-3KO chicken lymphocyte cell line has been used for last two decades to probe $IP_3R$ biology, we have recently used CRISPR/Cas9 technology to disrupt all three $IP_3R$ genes in human embryonic kidney (HEK293) cells to generate $IP_3R$ *null* HEK293 cells (HEK-3KO) (57). Tangible advantages of these cells include their mammalian origin, with presumably more relevant cellular milieu in terms of potential regulatory factors, and that HEK293 cells can be easily maintained and transfected. Therefore, we next asked if the R269W mutant behaves similarly in HEK-3KO compared with DT40 cells. Stable HEK-3KO cell lines were generated expressing WT $rIP_3R1$, $rIP_3R1^{RW}$, or $hIP_3R1^{RW}$ (Fig. 4*A*). Stable expression resulted in an obvious reticular pattern of expression, not obviously different from the localization of WT $IP_3R1$ (Fig. 4*B*). Expression of $rIP_3R1^{RW}$ did not result in alteration of the apparent content of the ER $Ca^{2+}$ store, as assessed by the $Ca^{2+}$ released following exposure to a SERCA pump inhibitor in a $Ca^{2+}$-free

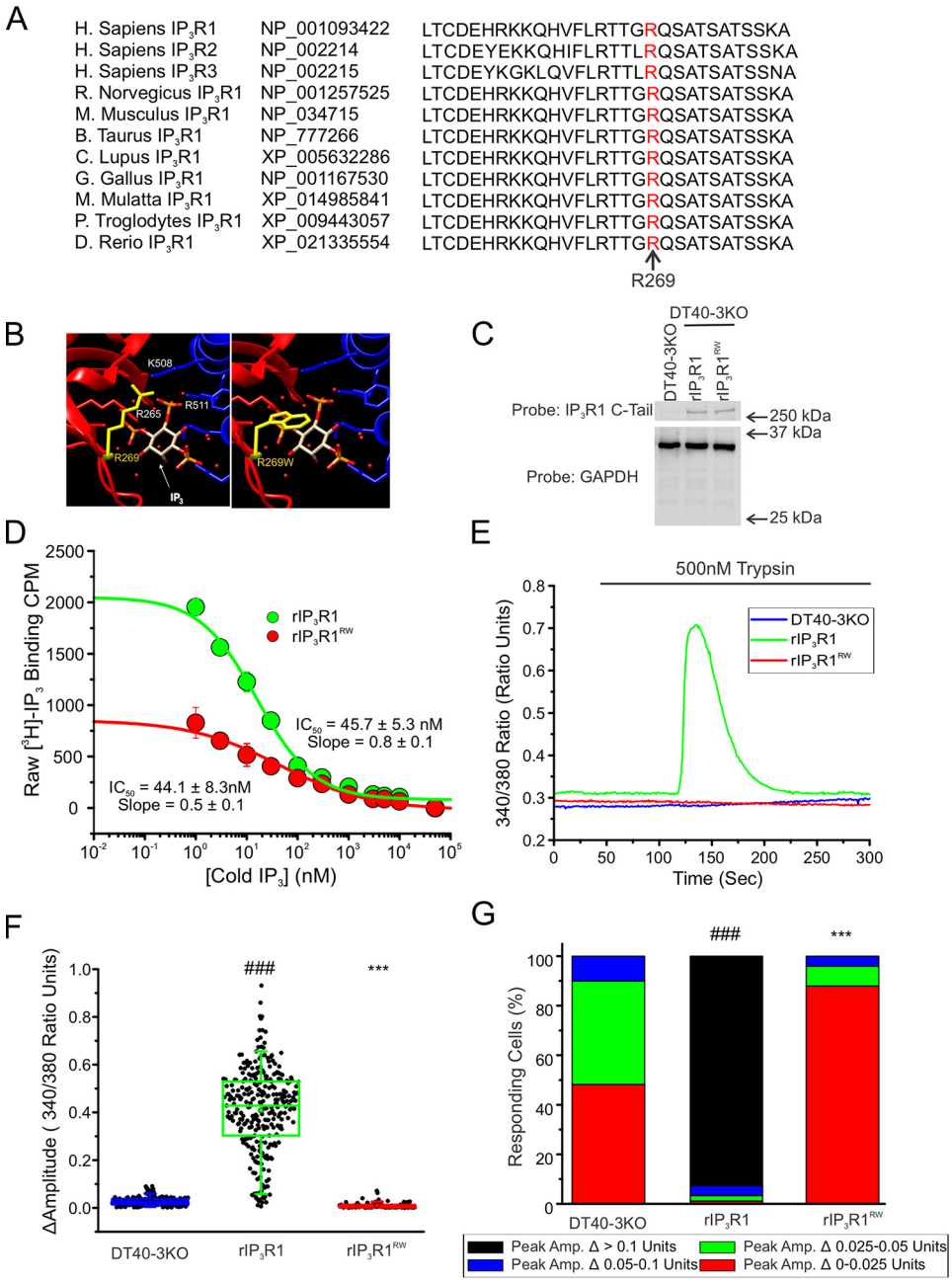


**Figure 2. rIP3R1RW is nonfunctional when expressed in DT40-3KO due to decreased IP3 binding.** *A,* Arg-269 (*red*) is conserved among all three human IP$_3$R isoforms and evolutionarily conserved in the IP$_3$R1 isoform. *B,* chimera (PDB code 3JAV) was used to visualize WT Arg-269 (*yellow*, *left panel*) and R269W mutant Trp-269 (*yellow*, *right panel*) interacting with IP$_3$ in the ligand binding cleft. *C,* WT rIP$_3$R1 and mutant rIP$_3$R1$^{RW}$ cell lines were generated in the IP$_3$R-null DT40-3KO cells and Western blotted. *D,* binding of 2.5 nM [$^3$H]IP$_3$ to WT rIP$_3$R1 and rIP$_3$R1$^{RW}$ in the presence of increasing concentrations (0 nM , 1 nM, 3 nM, 10 nM, 30 nM, 100 nM, 300 nM, 1 $\mu$M, 3 $\mu$M, 5 $\mu$M, 10 $\mu$M, and 50 $\mu$M) of cold IP$_3$ in a competitive radioligand-binding assay. Data are mean ± S.E. of three ($n = 3$) independent experiments. *E,* representative traces show $Ca^{2+}$ signals of IP$_3$R-null DT40-3KO cells (*blue*), WT rIP$_3$R1 (*green*), and rIP$_3$R1$^{RW}$ (*red*) in response to trypsin (500 nM) when loaded with Fura-2/AM. *F,* scatter plots summarizing change in amplitude (peak ratio – basal ratio: average of initial 5 ratio points) for experiments similar to those shown in *E*. *Boxes* represent the 25th, 50th, and 75th percentiles, whereas whiskers represent 5th and 95th percentiles and mean is represented by *colored circles*. *G,* stacked bar graph summarizing the percentage of amplitudes from *F*, which fall into pre-determined ranges such that only those cells with an amplitude change greater than 0.1 ratio units (*black* portion of bars) are considered to be responding to the trypsin stimulus shown in *E*. Unless otherwise stated, all data above comes from at least $n = 3$ experiments. ***, $p < 0.001$ when compared with WT rIP$_3$R1 cell line and ###, $p < 0.001$ when compared with DT40-3KO cell line; one-way ANOVA with Tukey's test performed in *F* ($F_{19,4699} = 753.0$, $p < 0.0001$) and *G* ($F_{19,50} = 284.6$, $p < 0.0001$).

extracellular buffer (Fig. S2, *A* and *B*). See supplemental experimental procedures. In single cell assays, stimulation of HEK-3KO expressing WT rIP$_3$R1 with 5, 50, or 500 nM trypsin generated robust $Ca^{2+}$ release (Fig. 4, *C* and *D*) with nearly 100% of cells responding (Fig. 4*E*). Notably, stimulation of cells expressing rIP$_3$R1$^{RW}$ also resulted in measurable $Ca^{2+}$ increases (Fig. 4, *C* and *D*), albeit, at much lower maximal amplitudes and with a lower percentage of responding cells responding (Fig. 4*E*). A small increase in amplitude was likewise seen in other clonal cell lines expressing rIP$_3$R1$^{RW}$ and hIP$_3$R$^{RW}$ in HEK-3KO cells (data not shown). These findings were recapitulated in populations of cells where [$Ca^{2+}$] changes were monitored in response

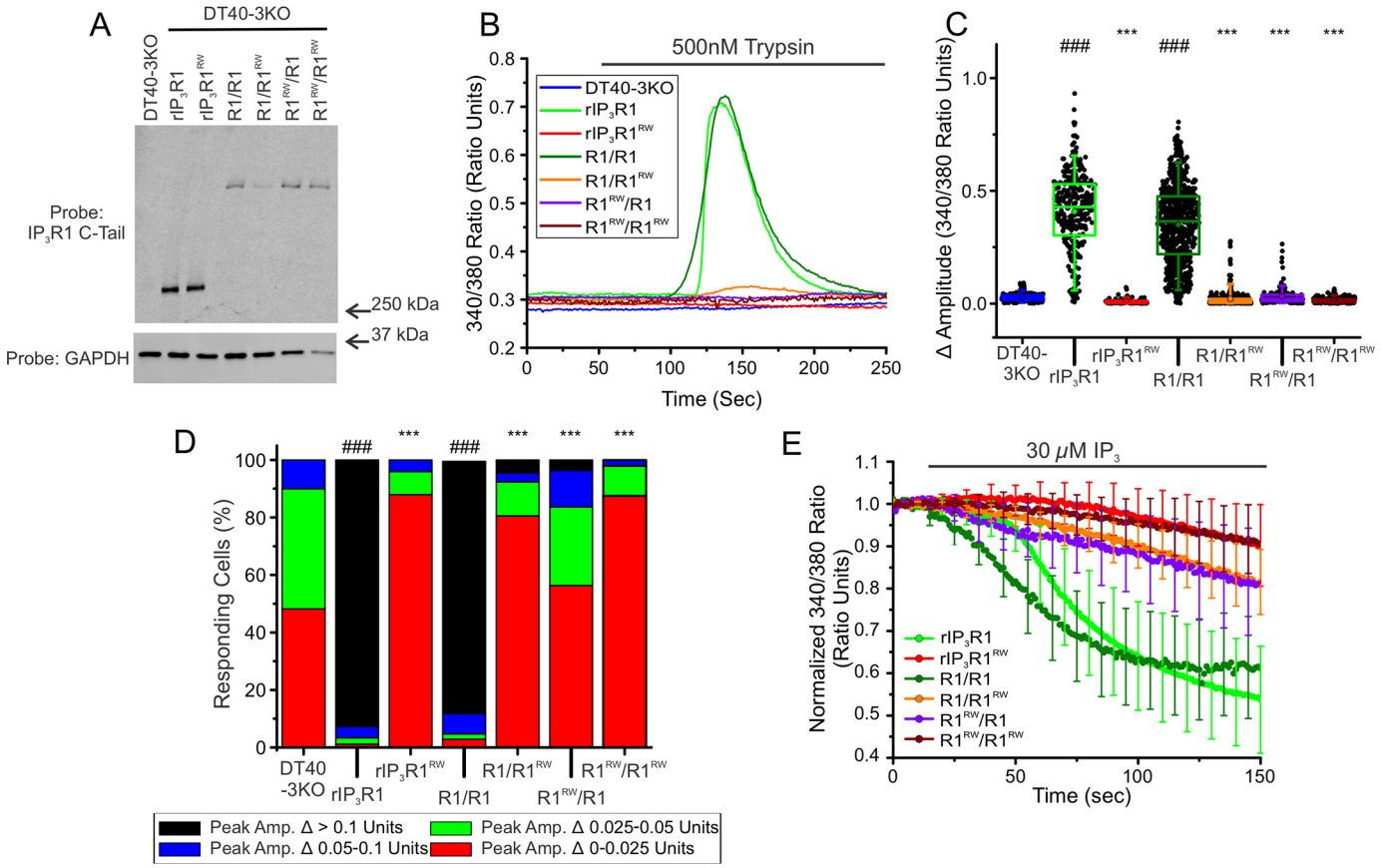


**Figure 3. Heterotetramers of WT rIP$_3$R1 and rIP$_3$R1$^{RW}$ are predominantly nonfunctional when expressed in DT40-3KO.** *A,* monomeric WT rIP$_3$R1 and mutant rIP$_3$R1$^{RW}$ cell lines, as well as dimeric R1/R1, R1/R1$^{RW}$, R1$^{RW}$/R1, and R1$^{RW}$/R1$^{RW}$ cell lines were generated in the IP$_3$R-null DT40-3KO cells and Western blotted. *B,* representative traces show $Ca^{2+}$ signals of IP$_3$R-null DT40-3KO cells (*blue*), WT rIP$_3$R1 (*green*), and rIP$_3$R1$^{RW}$ (*red*), R1/R1 (*dark green*), R1/R1$^{RW}$ (*orange*), R1$^{RW}$/R1 (*purple*), and R1$^{RW}$/R1$^{RW}$ (*dark red*) in response to trypsin (500 nM) when loaded with Fura-2/AM. *C,* scatter plots summarizing change in amplitude (peak ratio – basal ratio: average of initial 5 ratio points) for experiments similar to those shown in *B*. *Boxes* represent the 25th, 50th, and 75th percentiles, whereas whiskers represent 5th and 95th percentiles and mean is represented by *colored circles*. *D,* stacked bar graph summarizing the percentage of amplitudes from *C,* which fall into pre-determined ranges such that only those cells with an amplitude change greater than 0.1 ratio units (*black* portion of bars) are considered to be responding to the trypsin stimulus shown in *B*. *E,* traces show $Ca^{2+}$ signals of β-escin permeabilized WT rIP$_3$R1 (*green*), and rIP$_3$R1$^{RW}$ (*red*), R1/R1 (*dark green*), R1/R1$^{RW}$ (*orange*), R1$^{RW}$/R1 (*purple*), and R1$^{RW}$/R1$^{RW}$ (*dark red*) cell lines in response to IP$_3$ (30 μM) when loaded with Mag-Fura-2/AM. Data are mean ± S.E. of three ($n = 3$) independent experiments. Data for DT40-3KO, rIP$_3$R1, and rIP$_3$R1$^{RW}$ in *B–D* were from Fig. 2. Unless otherwise stated, all data above comes from at least $n = 3$ experiments. ***, $p < 0.001$ when compared with WT rIP$_3$R1 cell line and ###, $p < 0.001$ when compared with DT40-3KO cell line; one-way ANOVA with Tukey's test was performed in *C* ($F_{19,4699} = 753.0$, $p < 0.0001$) and *D* ($F_{19,50} = 284.6$, $p < 0.0001$).

to varying [trypsin] using a Flexstation3 plate reader (Fig. 4*F*). Additionally, the corresponding mutation in the human IP$_3$R1 (hIP$_3$R1$^{RW}$) stably expressed in HEK-3KO cells displayed a similar marked loss of function when compared with trypsin-induced release evoked in HEK-3KO cells stably expressing hIP$_3$R1 (Fig. 4*F*). The seemingly disparate findings obtained upon expression of R269W mutations in DT40-3KO and HEK-3KO could reflect differences in stable expression level of the mutant IP$_3$R in HEK-3KO cells compared with DT40-3KOs (Fig. S3*A*). In total, these findings show in two expression systems that R269W exhibits compromised IP$_3$ binding that results in severely reduced channel activity.

### *Mutation of N602D attenuates IP$_3$R1 activity without altering IP$_3$ binding*

The N602D mutation in IP$_3$R1 has been identified in two unrelated families and is associated with diagnoses of ataxic cerebral palsy without cerebral atrophy (48) and autosomal dominant congenital nonprogressive spinocerebellar ataxia (47, 52) (Table S1). Asn-602 is conserved among the three IP$_3$R subtypes and across many species (Fig. 5*A*). The residue is located just outside of the LBD, but formally within the IRBIT-binding domain (Table S3) and serves to connect two α-helical regions of the receptor (Fig. 5*B*). The mutation introduces a negatively charged residue at this site, replacing an asparagine residue with a polar neutral side chain with an aspartate residue harboring a polar acidic side chain. DT40-3KO cells stably expressing WT rIP$_3$R1 or rIP$_3$R1 expressing N602D (rIP$_3$R1$^{ND}$) mutations were generated (Fig. 5*C*). To establish the effects of this mutation on channel function, we first assessed IP$_3$ binding to the mutant proteins. In a competitive binding assay, rIP$_3$R1$^{ND}$ exhibited binding comparable with that of WT rIP$_3$R1, suggesting that the mutation does not interfere with IP$_3$ binding despite the proximity of the mutation to the LBD (Fig. 5*D*). To examine the consequences of the mutation on $Ca^{2+}$ release activities, cells expressing WT rIP$_3$R1 or rIP$_3$R1$^{ND}$ were stimulated with the PAR agonist, trypsin. Trypsin did not elicit any measurable [$Ca^{2+}$] increase in cells expressing rIP$_3$R1$^{ND}$ (Fig. 5*E*). The pooled data demonstrates that in terms of the magnitude of signal (Fig.

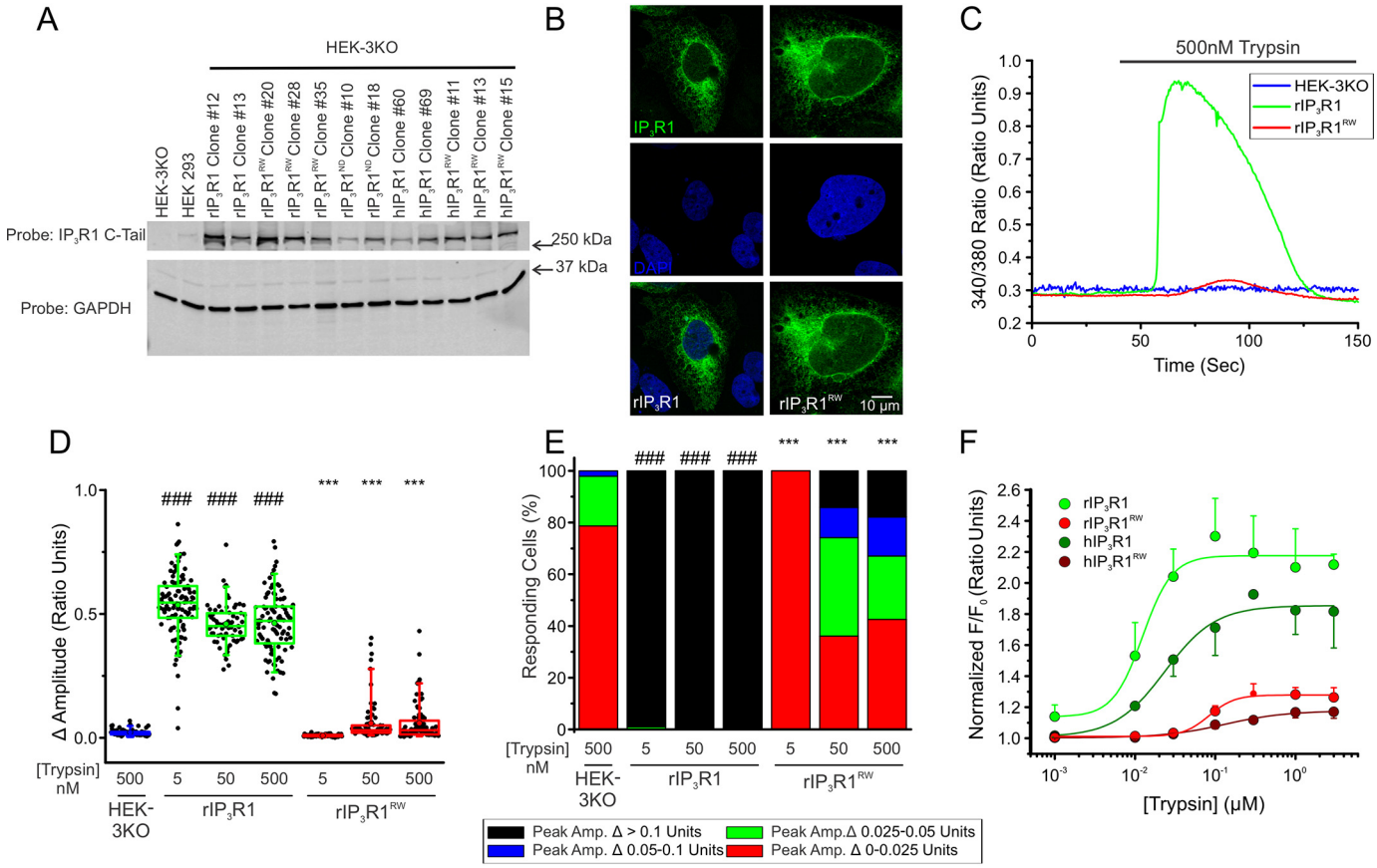


**Figure 4. rIP$_3$R1$^{RW}$ is poorly functional when expressed in HEK-3KO.** *A,* multiple WT rIP$_3$R1, WT hIP$_3$R1, mutant rIP$_3$R1$^{RW}$, mutant rIP$_3$R1$^{ND}$, and mutant hIP$_3$R1$^{RW}$ cell lines were generated in the IP$_3$R-null HEK-3KO cells and Western blotted. *B,* immunocytochemistry for HEK-3KO cell lines expressing either WT rIP$_3$R1 (*left*) or mutant rIP$_3$R1$^{RW}$ (*right*). *Top*, IP$_3$R1 detection (*green*); *middle*, DAPI detection (*blue*); *bottom*, merged images of IP$_3$R1 and DAPI. *Scale bars*, 10 $\mu$M. *C,* representative traces show $Ca^{2+}$ signals of IP$_3$R-null HEK-3KO cells (*blue*), WT rIP$_3$R1 (*green*), and rIP$_3$R1$^{RW}$ (*red*) in response to trypsin (500 nM) when loaded with Fura-2/AM. *D,* scatter plots summarizing change in amplitude (peak ratio – basal ratio: average of initial 5 ratio points) for experiments similar to those shown in *C* when treated with 5, 50, and 500 nM of trypsin. *Boxes* represent the 25th, 50th, and 75th percentiles, whereas whiskers represent 5th and 95th percentiles and mean is represented by *colored circles*. *E,* stacked bar graph summarizing the percentage of amplitudes from *D,* which fall into pre-determined ranges such that only those cells with an amplitude change greater than 0.1 ratio units (*black* portion of bars) are considered to be responding to the trypsin stimulus shown in *C*. *F,* dose-response curve showing $Ca^{2+}$ response of Fura-2/AM-loaded WT rIP$_3$R1, WT hIP$_3$R1, rIP$_3$R1$^{RW}$, and hIP$_3$R1$^{RW}$ cells when treated with increasing concentrations (1 nM, 10 nM, 30 nM, 100 nM, 300 nM, 1 $\mu$M, and 3 $\mu$M) of trypsin using a Flexstation3 96-well–plate reader. Data are mean ± S.E. of three ($n = 3$) independent experiments. ***, $p < 0.001$ when compared with WT rIP$_3$R1 cell line and ###, $p < 0.001$ when compared with HEK-3KO cell line; one-way ANOVA with Tukey's test was performed in *D* ($F_{15,1352} = 407.1$, $p < 0.0001$) and *E* ($F_{15,34} = 108.5$, $p < 0.0001$). Unless otherwise stated, all data above comes from at least $n = 3$ experiments.

5*F*), and the number of cells that respond above a defined threshold (Fig. 5*G*), rIP$_3$R1$^{ND}$ is refractory to stimulation in DT40-3KO cells.

Given, that the rIP$_3$R1$^{RW}$ mutation exhibited more activity when stably expressed in HEK-3KO cells when compared with DT40-3KOs, we next investigated whether rIP$_3$R1$^{ND}$ was similarly more active when stably expressed in this mammalian cell line (Fig. 6*A*). Expression of rIP$_3$R1$^{ND}$ in HEK-3KO cells did not result in alteration of the apparent content of the ER $Ca^{2+}$ store (Fig. S2*C*) and resulted in an obvious reticular pattern of expression (Fig. S4). Consistent, with data obtained in cells expressing rIP$_3$R1$^{RW}$, stimulation of single HEK-3KO stably expressing rIP$_3$R1$^{ND}$ with various [trypsin] resulted in modest $Ca^{2+}$ release (Fig. 6*B*) manifested as reduced maximal initial release (Fig. 6*C*) and a lower percentage of cells responding at all [trypsin] (Fig. 6*D*). Once again, differences observed when the mutant is stably expressed in HEK-3KO cells compared with DT40-3KOs may result from differences in mutant protein expression in the two cell lines (Fig. S3*B*). A mutation in a neighboring residue in the same region, Thr-594 (T594I) (Fig. S5*A*), which is associated with infantile onset SCA (49), exhibited a similar decreased $Ca^{2+}$ release (Fig. S5*D*) and percentage of cells responding (Fig. S5*E*) when stably expressed in HEK-3KO cells (Fig. S5*B*) and stimulated with a maximal concentration of trypsin (Fig. S5*C*). Reflecting the behavior at the single cell level, in population assays, the concentration *versus* response relationship for trypsin-induced [$Ca^{2+}$] release reflected a decrease in both efficacy and sensitivity of stimulation (Fig. 6*E* and Fig. S5*F*). Thus, although competent to bind IP$_3$, homomeric IP$_3$R1 harboring mutations in this region are largely nonfunctional.

We next investigated the impact of the presence of variable numbers of mutant rIP$_3$R1$^{ND}$ within a heterotetrametric assembly of subunits, which likely represents the situation in patients heterozygous for the mutation. Once again, the IP$_3$R1 protein was readily detected in samples immunoprecipitated with a mCherry antibody suggesting heterotetrameric channels containing both WT and mutant channels are formed (Fig. S1*A*). Concatenated dimers were generated containing one

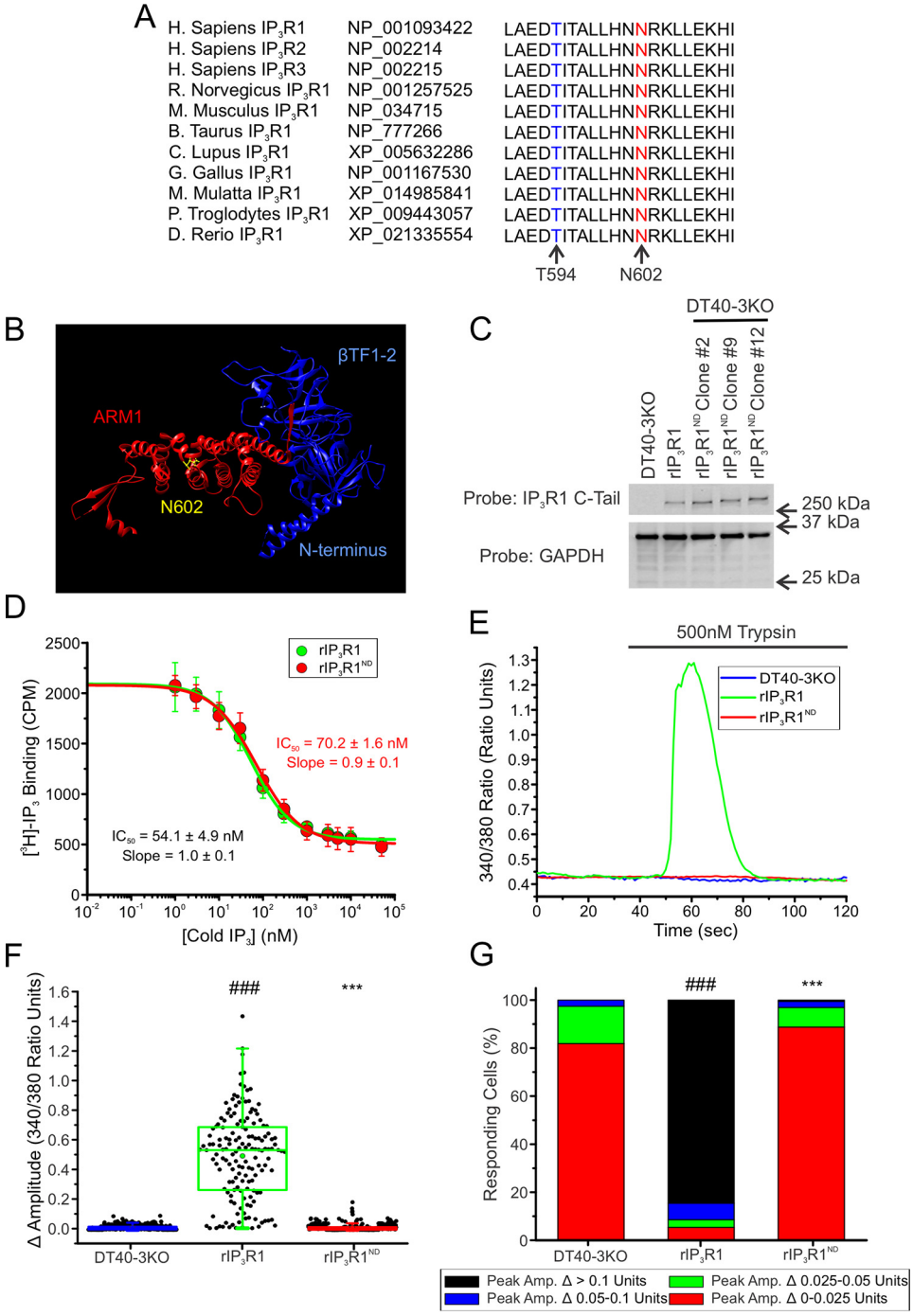


**Figure 5. rIP$_3$R1$^{ND}$ is nonfunctional when expressed in DT40-3KO.** *A,* Asn-602 (*red*) and Thr-594 (*blue*) are conserved among all three human IP$_3$R isoforms and evolutionarily conserved in the IP$_3$R1 isoform. *B,* chimera (PDB 6MU1) was used to visualize WT Asn-602 (*yellow*) between two $\alpha$-helical regions in the ARM1 domain (*red*) and adjacent to the $\beta$-TF1 and $\beta$-TF2 domains in the N terminus (*blue*). *C,* WT rIP$_3$R1 and several mutant rIP$_3$R1$^{ND}$ cell lines generated in the IP$_3$R-null DT40-3KO cells were Western blotted. *D,* binding of 2.5 nM [$^3$H]IP$_3$ to WT rIP$_3$R1 (*green*) and rIP$_3$R1$^{ND}$ (*red*) in the presence of increasing concentrations (0 nM, 1 nM, 3 nM, 10 nM, 30 nM, 100 nM, 300 nM, 1 $\mu$M, 3 $\mu$M, 5 $\mu$M, 10 $\mu$M, and 50 $\mu$M) of cold IP$_3$ in a competitive radioligand binding assay. Data are mean ± S.E. of three ($n = 3$) independent experiments. *E,* representative traces show $Ca^{2+}$ signals of IP3R-null DT40-3KO cells (*blue*), WT rIP$_3$R1 (*green*), and rIP$_3$R1$^{ND}$ (*red*) in response to trypsin (500 nM) when loaded with Fura-2/AM. *F,* scatter plots summarizing change in amplitude (peak ratio – basal ratio: average of initial 5 ratio points) for experiments similar to those shown in *E*. *Boxes* represent the 25th, 50th, and 75th percentiles, whereas whiskers represent 5th and 95th percentiles and mean is represented by *colored circles*. *G,* stacked bar graph summarizing the percentage of amplitudes from *F*, which fall into pre-determined ranges such that only those cells with an amplitude change greater than 0.1 ratio units (*black* portion of bars) are considered to be responding to the trypsin stimulus shown in *E*. Unless otherwise stated, all data above comes from at least $n = 3$ experiments. ***, $p < 0.001$ when compared with WT rIP3R1 cell line and ###, $p < 0.001$ when compared with DT40-3KO cell line; one-way ANOVA with Tukey's test was performed in F ($F_{7,3070} = 525.9$, $p < 0.0001$) and *G* ($F_{9,19} = 177.2$, $p < 0.0001$).

WT rIP$_3$R1 and one rIP$_3$R1$^{ND}$ (rIP3R1-rIP$_3$R1$^{ND}$: R1/R1$^{ND}$ or rIP$_3$R1$^{ND}$-rIP$_3$R1: R1/R1$^{ND}$) and stably expressed in DT40-3KO cells (Fig. 7*A*). As shown previously, tetramers expressed from either monomeric rIP$_3$R1 (WT rIP$_3$R1) or dimeric rIP$_3$R1 (R1/R1) were capable of supporting robust PAR2-mediated $Ca^{2+}$ signaling, however, tetramers assembled from R1$^{ND}$/R1

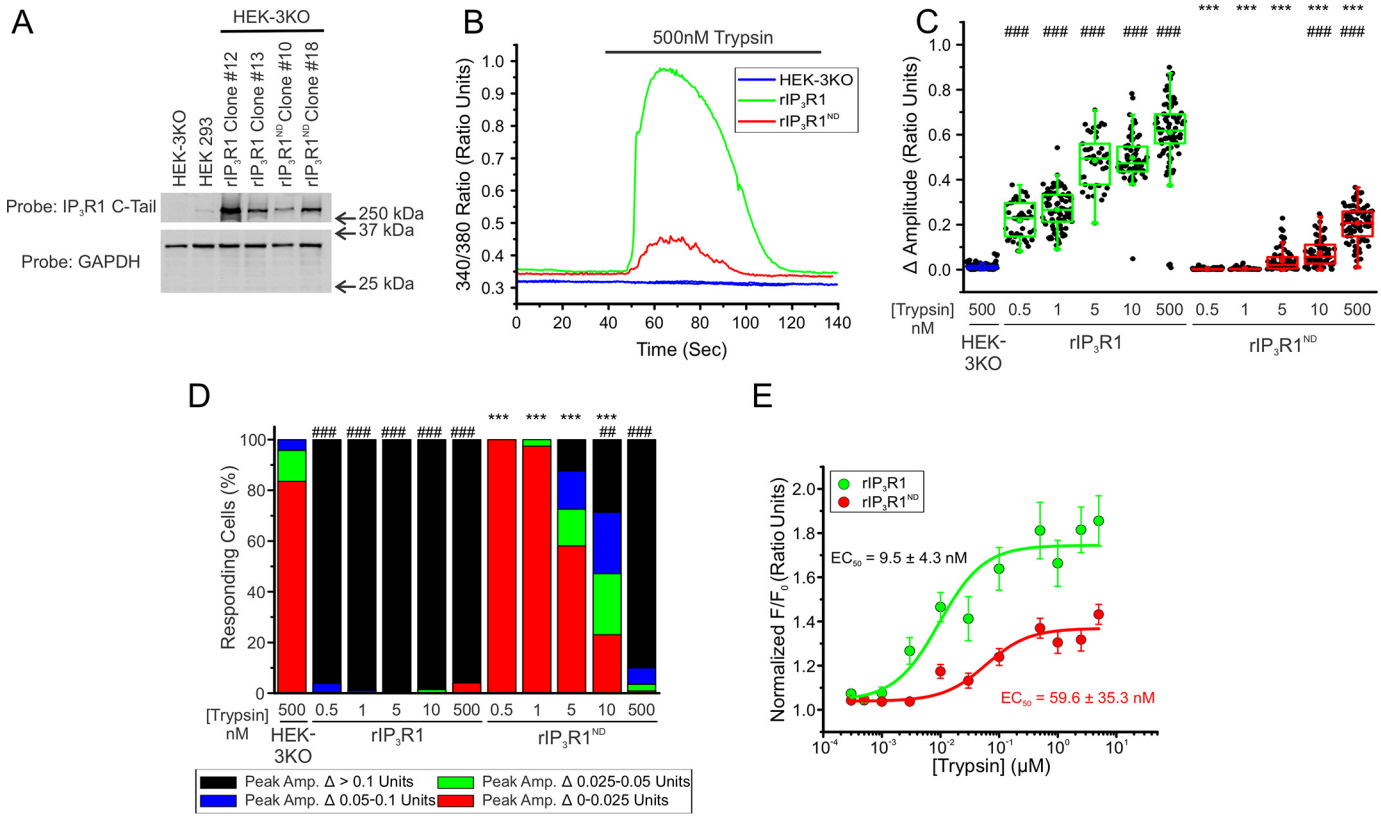


**Figure 6. rIP$_3$R1$^{ND}$ is poorly functional when expressed in HEK-3KO.** *A,* multiple WT rIP3R1 and mutant rIP$_3$R1$^{ND}$ cell lines were generated in the IP$_3$R-null HEK-3KO cells and Western blotted. *B,* representative traces show $Ca^{2+}$ signals of IP3R-null HEK-3KO cells (*blue*), WT rIP$_3$R1 (*green*), and rIP$_3$R1$^{ND}$ (*red*) in response to trypsin (500 nM) when loaded with Fura-2/AM. *C,* scatter plots summarizing change in amplitude (peak ratio – basal ratio: average of initial 5 ratio points) for experiments similar to those shown in *B* when treated with 0.5, 1, 10, and 500 nM trypsin. *Boxes* represent the 25th, 50th, and 75th percentiles, whereas whiskers represent 5th and 95th percentiles and mean is represented by *colored circles*. *D,* stacked bar graph summarizing the percentage of amplitudes from *C,* which fall into pre-determined ranges such that only those cells with an amplitude change greater than 0.1 ratio units (*black* portion of bars) are considered to be responding to the trypsin stimulus shown in *B*. *E,* dose-response curve showing $Ca^{2+}$ response of Fura-2/AM-loaded WT rIP$_3$R1 and rIP$_3$R1$^{ND}$ cells when treated with increasing concentrations (0.5 nM, 1 nM, 3 nM, 10 nM, 30 nM, 100 nM, 300 nM, 500 nM, 1 μM, 2.5 μM, and 5 μM) of trypsin using a Flexstation3 96-well–plate reader. Data are mean ± S.E. of three ($n = 3$) independent experiments. **, $p < 0.01$ and ***, $p < 0.001$ when compared with WT rIP$_3$R1 cell line and ###, $p < 0.001$ when compared with HEK-3KO cell line; one-way ANOVA with Tukey's test was performed in *C* ($F_{10,791} = 532.1$, $p < 0.0001$) and *D* ($F_{10,22} = 108.6$, $p < 0.0001$). Unless otherwise stated, all data above comes from at least $n = 3$ experiments.

or R1/R1$^{ND}$ were completely refractory to stimulation at maximal [trypsin] (Fig. 7, *B–D*). These data indicate that tetramers harboring two mutant IP$_3$R1$^{ND}$ subunits are likely severely compromised even given the modest activity of this mutant in HEK cells. To investigate if tetramers harboring only a single mutant rIP$_3$R1$^{ND}$ retain any activity, concatenated tetramers were generated with three WT rIP$_3$R1 and one rIP$_3$R1$^{ND}$ (rIP$_3$R1-rIP$_3$R1-rIP$_3$R1-rIP$_3$R1$^{ND}$: R1/R1/R1/R1$^{ND}$) and stably expressed in DT40-3KO cells (Fig. 7*E*). Notably, some cells expressing R1/R1/R1/R1$^{ND}$ tetramers retained a comparable ability to support $Ca^{2+}$ release to a concatenated tetramer assembled from WT rIP$_3$R1 in terms of both trypsin (Fig. 7, *F–H*) and IP$_3$-evoked $Ca^{2+}$ release (Fig. 7*I*). In total these data demonstrate that rIP$_3$R$^{ND}$ retains modest activity and that tetramers harboring this gating mutant are not necessarily completely disabled.

### *Mutation of G2498S in the channel pore attenuates IP$_3$R2 activity*

We next investigated a missense mutation (G2498S) in IP$_3$R2, identified in a family with generalized anhidrosis (55). IP$_3$R2 is the predominant IP$_3$R isoform expressed in eccrine sweat glands. Homozygous individuals were reported to have morphologically normal eccrine sweat glands but suffer from severe hyperthermia resulting from an absence of perspiration in response to physiological or pharmacological stimuli (Table S1). Notably, however, heterozygous siblings did not exhibit any symptoms of disease and thus this mutation represents a rare example of autosomal recessive inheritance of disease symptoms associated with IP$_3$R mutations. The Gly-2498 residue in IP$_3$R2 is located in a motif (GGG*X*G) conserved in all IP$_3$R subtypes (Fig. 8*A*) as well as the superfamily of cation channels and forms the selectivity filter of the ion conducting pathway (Fig. 8*B*). This ion permeability pathway is a hot spot of other disease-associated mutations in multiple IP$_3$R types (Table S4). This mutation (G2498S; designated mIP$_3$R2$^{GS}$) substitutes an evolutionarily conserved, nonpolar, hydrophobic, glycine residue, with a polar, hydrophillic serine residue and thus might reasonably be expected to disrupt the pore of the channel. Consistent with previous studies, when stably expressed in DT40-3KO cells (Fig. 8*C*), IP$_3$ binding to mIP$_3$R2$^{GS}$ was comparable with WT mIP$_3$R2 (Fig. 8*D*). Nevertheless, trypsin stimulation failed to elicit any $Ca^{2+}$ release in these cells (Fig. 8, *E–G*). Again, stable expression of

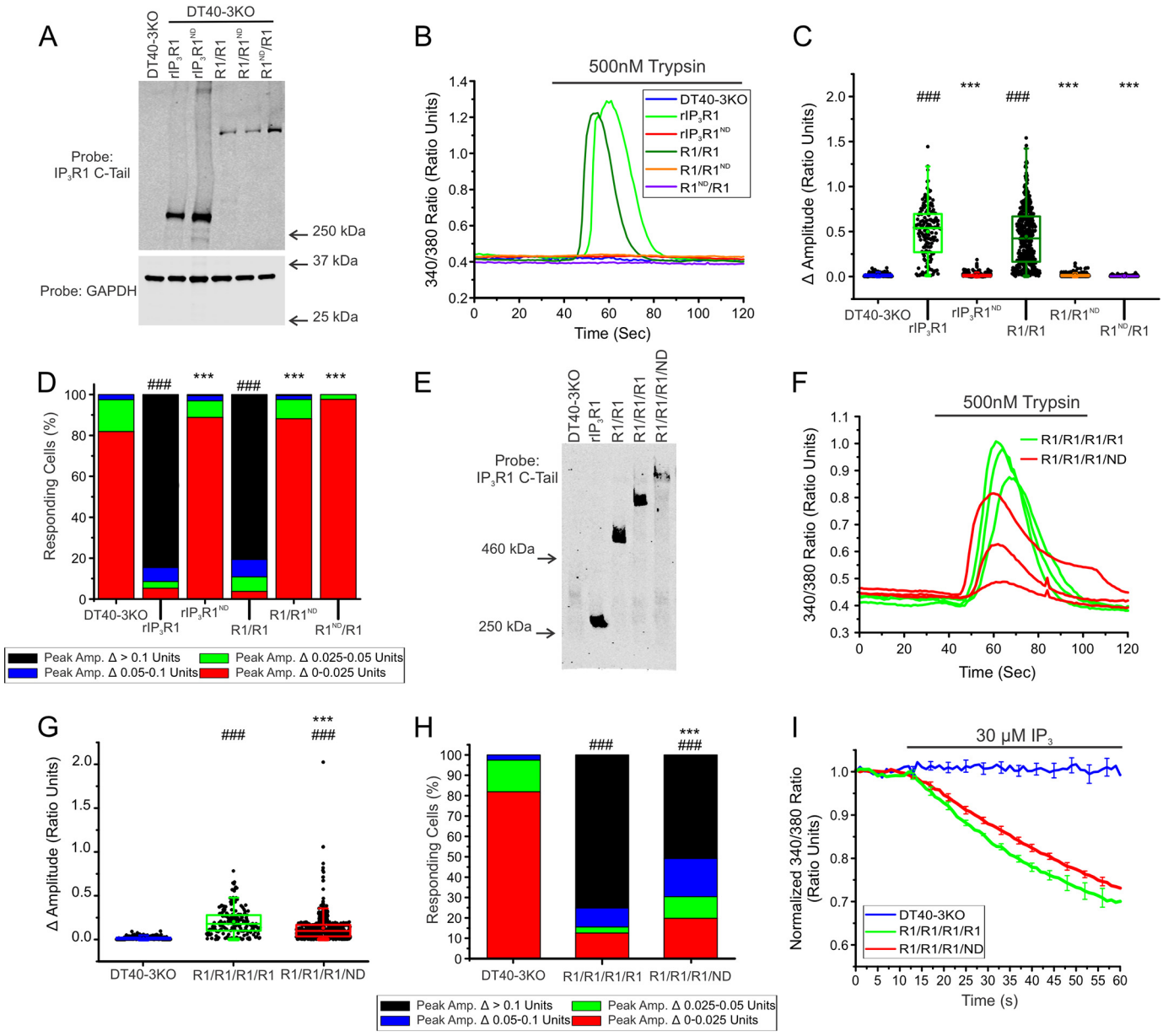


**Figure 7. Heterotetramers of WT rIP$_3$R1 and rIP$_3$R1$^{ND}$ are predominantly nonfunctional when expressed in DT40-3KO.** *A,* monomeric WT rIP$_3$R1 and mutant rIP$_3$R1$^{ND}$ cell lines, as well as dimeric R1/R1, R1/R1$^{ND}$, and R1$^{ND}$/R1 cell lines were generated in the IP$_3$R-null DT40-3KO cells and Western blotted. *B,* representative traces show $Ca^{2+}$ signals of IP$_3$R-null DT40-3KO cells (*blue*), WT rIP$_3$R1 (*green*), and rIP$_3$R1$^{ND}$ (*red*), R1/R1 (*dark green*), R1/R1$^{ND}$ (*orange*), and R1$^{ND}$/R1 (*purple*) in response to trypsin (500 nM) when loaded with Fura-2/AM. *C,* scatter plots summarizing the change in amplitude (peak ratio – basal ratio: average of initial 5 ratio points) for experiments similar to those shown in *B. Boxes* represent the 25th, 50th, and 75th percentiles, whereas whiskers represent the 5th and 95th percentiles and the mean is represented by *colored circles*. *D,* stacked bar graph summarizing the percentage of amplitudes from *C*, which fall into pre-determined ranges such that only those cells with an amplitude change greater than 0.1 ratio units (*black* portion of bars) are considered to be responding to the trypsin stimulus shown in *B. E,* monomeric WT rIP3R1, dimeric R1/R1, trimeric R1/R1/R1, and tetrameric R1/R1/R1/ND cell lines generated in the IP3R-null DT40-3KO cells were Western blotted. *F,* multiple representative traces show $Ca^{2+}$ signals of IP3R-null DT40-3KO cells expressing R1/R1/R1/R1 (*green*) and R1/R1/R1/ND (*red*) tetramers in response to trypsin (500 nM) when loaded with Fura-2/AM. *G,* scatter plots summarizing change in amplitude for experiments similar to those shown in *F* when treated with 500 nM trypsin. *H,* stacked bar graph summarizing the percentage of amplitudes from *G*, which fall into pre-determined ranges such that only those cells with an amplitude change greater than 0.1 ratio units (*black* portion of bars) are considered to be responding to the trypsin stimulus shown in *F. I,* traces show $Ca^{2+}$ signals of β-escin permeabilized IP3R-null DT40-3KO cells (*blue*), R1/R1/R1/R1 (*green*), and R1/R1/R1/ND (*red*) cell lines in response to IP$_3$ (30 μM) when loaded with Mag-Fura-2/AM. Data are mean ± S.E. of three ($n = 3$) independent experiments. Data for rIP3R1 and rIP$_3$R1$^{ND}$ in *B–D* and DT40-3KO in *B–H* came from Fig. 5. Unless otherwise stated, all data above comes from at least $n = 3$ experiments. ***, $p < 0.001$ when compared with WT rIP3R1 cell line and ###, $p < 0.001$ when compared with DT40-3KO cell line; one-way ANOVA with Tukey's test was performed in *C* ($F_{7,3070} = 525.9$, $p < 0.0001$), *D* ($F_{9,19} = 177.2$, $p < 0.0001$), *G* ($F_{7,3070} = 525.9$, $p < 0.0001$), and *H* ($F_{9,19} = 177.2$, $p < 0.0001$).

mIP$_3$R2$^{GS}$ in HEK-3KO cells did not alter the apparent store content of the ER (Fig. S2*D*) and resulted in an obvious reticular pattern of expression (Fig. S4*B*). However, notably, in contrast to the previous mutations investigated, when expressed in HEK-3KO cells (Fig. 9*A*) mIP$_3$R2$^{GS}$ was unable to support any measurable $Ca^{2+}$ release (Fig. 9, *B–E*). Similar results were seen in other clonal lines expressing the G2498S mutations (data not shown), as well as HEK-3KO cells stably expressing a mutation in hIP$_3$R1 G2506R (Fig. S6, *A–F*), corresponding to the neighboring glycine in the

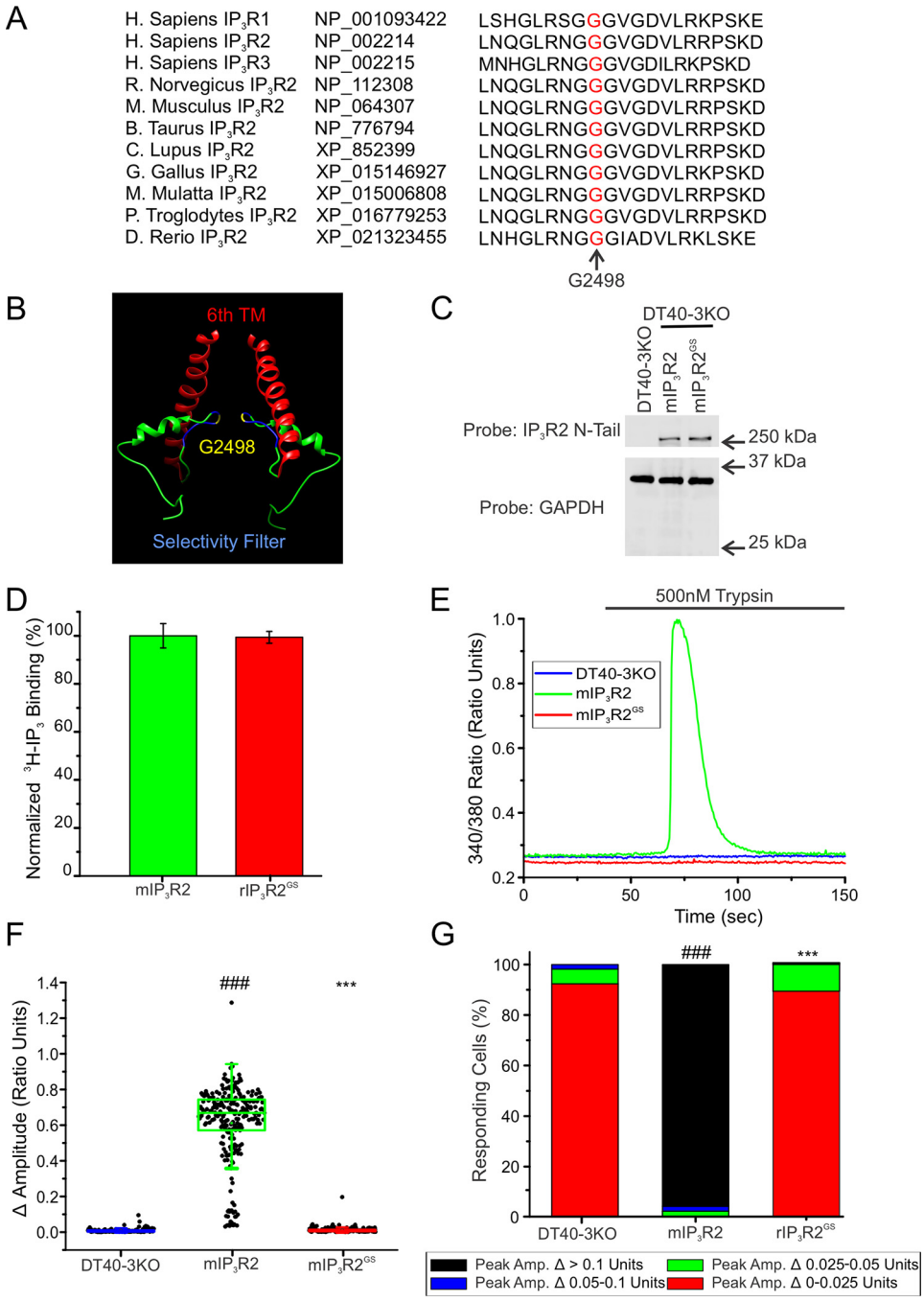


**Figure 8. mIP$_3$R2$^{GS}$ is nonfunctional when expressed in DT40-3KO.** *A,* Gly-2498 (*red*) is conserved among all three human IP3R isoforms and evolutionarily conserved in the IP$_3$R2 isoform. *B,* chimera (PDB 6MU1) was used to visualize WT Gly-2498 (*yellow*) in the selectivity filter (*blue*) of two monomers, just prior to the 6th transmembrane (*TM*) domain (*red*). *C,* WT mIP$_3$R2 and mutant mIP$_3$R2$^{GS}$ cell lines were generated in the IP$_3$R-null DT40-3KO cells and Western blotted. *D,* binding of 2.5 nM [$^3$H]IP$_3$ to WT mIP$_3$R2 and mIP$_3$R2$^{GS}$ in the presence of a maximal concentration of 50 $\mu$M cold IP$_3$ in a competitive radioligand binding assay ($p = 0.9077$). Data are mean ± S.E. of three ($n = 3$) independent experiments. *E,* representative traces show $Ca^{2+}$ signals of IP3R-null DT40-3KO cells (*blue*), WT mIP$_3$R2 (*green*), and mIP$_3$R2$^{GS}$ (*red*) in response to trypsin (500 nM) when loaded with Fura-2/AM. *F,* scatter plots summarizing change in amplitude (peak ratio – basal ratio: average of initial 5 ratio points) for experiments similar to those shown in *E*. *Boxes* represent the 25th, 50th, and 75th percentiles, whereas whiskers represent 5th and 95th percentiles and mean is represented by *colored circles*. *G,* stacked bar graph summarizing the percentage of amplitudes from *F,* which fall into pre-determined ranges such that only those cells with an amplitude change greater than 0.1 ratio units (*black* portion of bars) are considered to be responding to the trypsin stimulus shown in *E*. Unless otherwise stated, all data above comes from at least $n = 3$ experiments. ***, $p < 0.001$ when compared with WT rIP3R1 cell line and ###, $p < 0.001$ when compared with HEK-3KO cell line; unpaired *t* test was performed in *D* and one-way ANOVA with Tukey's test was performed in *F* ($F_{9,1568} = 437.7$, $p < 0.0001$) and *G* ($F_{9,27} = 61.27$, $p < 0.0001$).

GGG*X*G motif. This mutation is associated with spinocerebellar ataxia and Gillespie syndrome. Again, differences in expression in HEK-3KO cells *versus* DT40-3KO cells may in part explain these results (Fig. S3*C*). Overall, these data confirm that homozygous expression of mIP$_3$R2$^{GS}$ results in a complete abrogation of IP$_3$R activity and is consistent with the severe phenotype in individuals homozygous for the mutation.

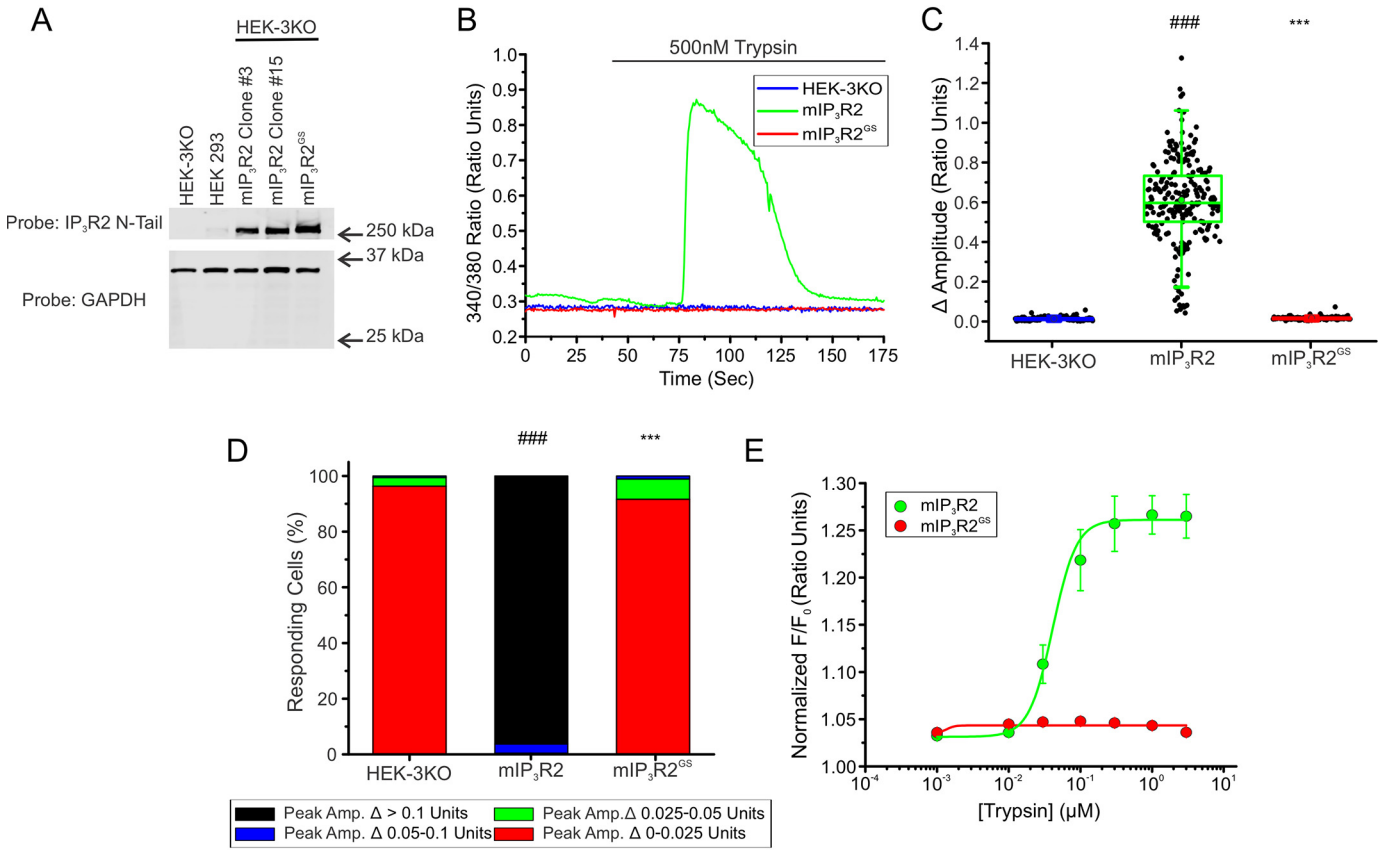


**Figure 9. mIP$_3$R2$^{GS}$ is predominantly nonfunctional when expressed in HEK-3KO.** *A*, multiple WT mIP$_3$R2 and mutant mIP$_3$R2$^{GS}$ cell lines were generated in the IP$_3$R-null HEK-3KO cells and Western blotted. *B*, representative traces show $Ca^{2+}$ signals of IP$_3$R-null HEK-3KO cells (*blue*), WT mIP$_3$R2 (*green*), and mIP$_3$R2$^{GS}$ (*red*) in response to trypsin (500 nM) when loaded with Fura-2/AM. *C*, scatter plots summarizing change in amplitude (peak ratio – basal ratio: average of initial 5 ratio points) for experiments similar to those shown in *B* when treated with 500 nM trypsin. *Boxes* represent the 25th, 50th, and 75th percentiles, whereas whiskers represent 5th and 95th percentiles and mean is represented by *colored circles*. *D*, stacked bar graph summarizing the percentage of amplitudes from *C*, which fall into pre-determined ranges such that only those cells with an amplitude change greater than 0.1 ratio units (*black* portion of bars) are considered to be responding to the trypsin stimulus shown in *B*. *E*, dose-response curve showing $Ca^{2+}$ response of Fura-2/AM-loaded WT mIP$_3$R2 and mIP$_3$R2$^{GS}$ cells when treated with increasing concentrations (1 nM, 10 nM, 30 nM, 100 nM, 300 nM, 1 $\mu$M, and 3 $\mu$M) of trypsin using a Flexstation3 96-well–plate reader. Data are mean ± S.E. of three ($n = 3$) independent experiments. ***, $p < 0.001$ when compared with WT rIP$_3$R1 cell line and ###, $p < 0.001$ when compared with HEK-3KO cell line; one-way ANOVA with Tukey's test was performed in *C* ($F_{6,809} = 707.1$, $p < 0.0001$) and *D* ($F_{6,17} = 335.6$, $p < 0.0001$). Unless otherwise stated, all data above comes from at least $n = 3$ experiments.

As the heterozygous siblings of the affected individuals were seemingly not markedly impacted by harboring the mutation, we next investigated the behavior of tetrameric channels assembled from WT and mIP$_3$R2$^{GS}$. Immunoprecipitation once again confirmed that mutated mIP$_3$R2$^{GS}$ monomers could interact with other monomeric subunits (Fig. S1, *B* and *C*). The current structural model based on the cryo-EM structure of IP$_3$R1 (PDB codes 6MU1 and 6MU2) indicates that the Ser substitution for Gly-2547 (Gly-2498 in IP$_3$R2) may form H bonds with the neighboring Arg-2544 residue (Fig. 10*A*), potentially resulting in constrained movement and restricted opening of the pore in a homotetramer harboring this mutant. Concatenated cDNA encoding either homodimeric mIP$_3$R2-mIP$_3$R2 (R2/R2) and mIP$_3$R2$^{GS}$-mIP$_3$R2$^{GS}$ (R2$^{GS}$/R2$^{GS}$) or heterodimeric IP$_3$R2$^{GS}$-IP$_3$R2 (R2$^{GS}$/R2 and R2/R2$^{GS}$) were generated and stably expressed in DT40-3KO cells (Fig. 10*B*). As shown previously (38), trypsin stimulation of cells expressing both mIP$_3$R2 and R2/R2 elicited vigorous $Ca^{2+}$ release (Fig. 10*C*). Although cells expressing R2$^{GS}$/R2$^{GS}$ were refractory to stimulation, surprisingly, stimulation of cells expressing R2$^{GS}$/R2 or R2/R2$^{GS}$ exhibited robust $Ca^{2+}$ release (Fig. 10*C* and pooled data in Fig. 10, *D* and *F*). This partial channel functionality was confirmed through stimulation of additional cell lines expressing R2$^{GS}$/R2 or R2/R2$^{GS}$ (data not shown). Similarly, exposure to IP$_3$ in permeabilized cells also evoked robust $Ca^{2+}$ release in WT homotetramers, intermediate $Ca^{2+}$ release in heterotetramers, and no $Ca^{2+}$ release in mutant homotetramers (Fig. 10*F*). These studies therefore reveal that heterotetrameric channels composed of two WT and two G2498S mutant subunits retain significant function as IP$_3$-sensitive channels. Our data suggest that substitution of two or fewer Gly-Ser results in less restriction of pore movement required for gating, such that significant $Ca^{2+}$ flux can occur that likely supports activity sufficient to render heterozygous individuals asymptomatic.

## Discussion

Mutations have been identified throughout human IP$_3$R genes and are associated with numerous diseases (58, 59). How these mutations affect channel function and contribute to the

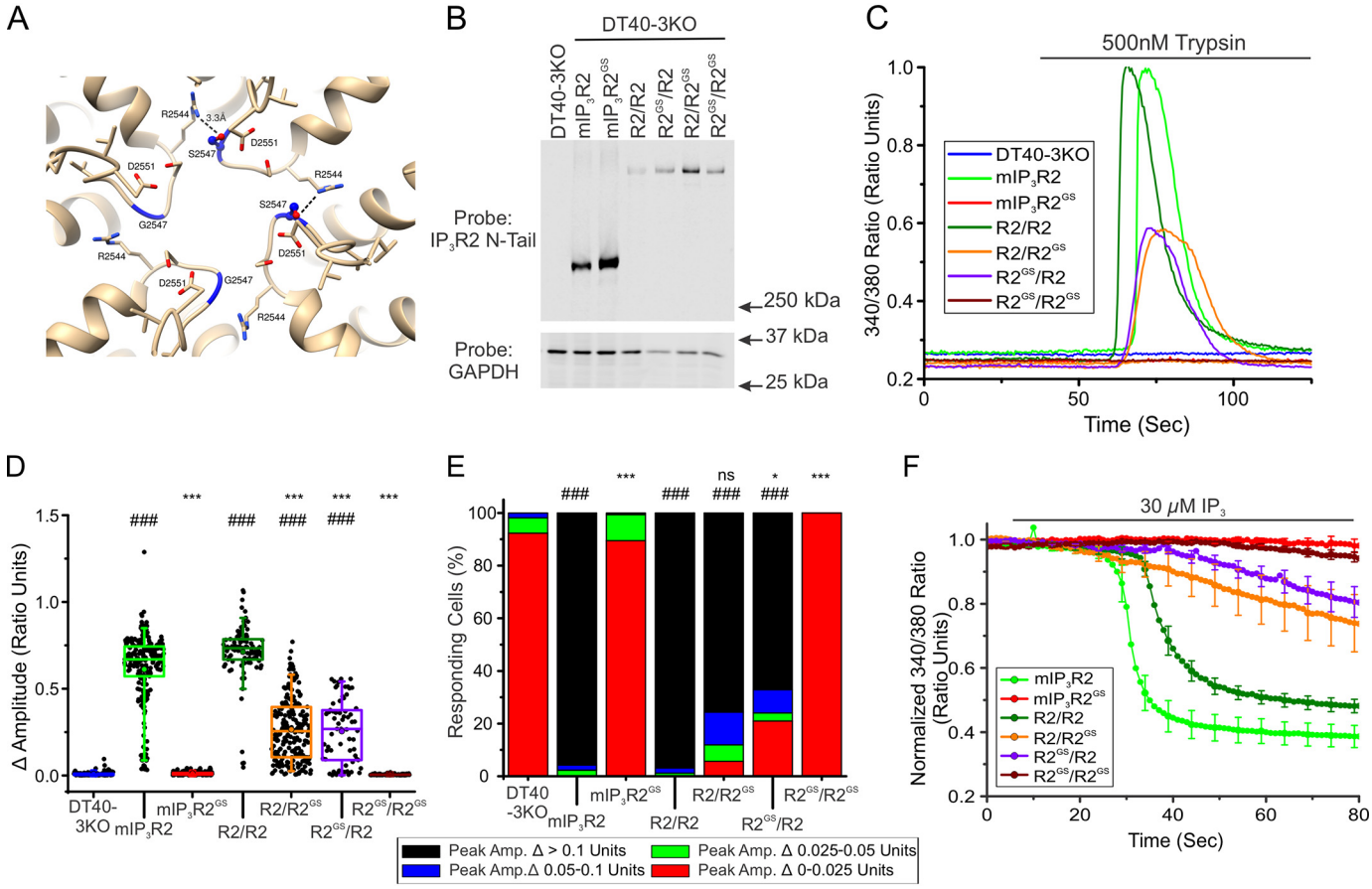


**Figure 10. Heterotetramers of WT mIP$_3$R2 and mIP$_3$R2$^{GS}$ retain partial functionality when expressed in DT40-3KO.** *A,* the current IP$_3$R structural model based on the cryo-EM structure of IP$_3$R1 (PDB codes 6MU1 and 6MU2) indicates that the G2498S substitution may form H bonds with neighboring Arg-2544. *B,* monomeric WT mIP$_3$R2 and mutant mIP$_3$R2$^{GS}$ cell lines, as well as dimeric R2/R2, R2/R2$^{GS}$, R2$^{GS}$/R2, and R2$^{GS}$/R2$^{GS}$ cell lines generated in the IP$_3$R-null DT40-3KO cells were Western blotted. *C,* representative traces show $Ca^{2+}$ signals of IP$_3$R-null DT40-3KO cells (*blue*), WT mIP$_3$R2 (*green*), and mIP$_3$R2$^{GS}$ (*red*), R2/R2 (*dark green*), R2/R2$^{GS}$ (*orange*), R2$^{GS}$/R2 (*purple*), and R2$^{GS}$/R2$^{GS}$ (*dark red*) in response to trypsin (500 nM) when loaded with Fura-2/AM. *D,* scatter plots summarizing change in amplitude (peak ratio – basal ratio: average of initial 5 ratio points) for experiments similar to those shown in *C. Boxes* represent the 25th, 50th, and 75th percentiles, whereas whiskers represent the 5th and 95th percentiles and mean is represented by *colored circles*. *E,* stacked bar graph summarizing the percentage of amplitudes from *D,* which fall into pre-determined ranges such that only those cells with an amplitude change greater than 0.1 ratio units (*black* portion of bars) are considered to be responding to the trypsin stimulus shown in *C*. *F,* traces show $Ca^{2+}$ signals of β-escin permeabilized WT mIP$_3$R2 (*green*), and mIP$_3$R2$^{GS}$ (*red*), R2/R2 (*dark green*), R2/R2$^{GS}$ (*orange*), R2$^{GS}$/R2 (*purple*), and R2$^{GS}$/R2$^{GS}$ (*dark red*) cell lines in response to IP$_3$ (30 μM) when loaded with Mag-Fura-2/AM. Data are mean ± S.E. of three ($n$ = 3) independent experiments. Data for DT40-3KO, mIP$_3$R2, and mIP$_3$R2$^{GS}$ in *D*–*F* came from Fig. 8. *, $p < 0.05$ and ***, $p < 0.001$ when compared with corresponding WT cell line (WT mIP$_3$R2 for monomers and R2/R2 cell line for dimers) and ###, $p < 0.001$ when compared with DT40-3KO cell line; one-way ANOVA with Tukey's test was performed in *D* ($F_{9,1568} = 437.7$, $p < 0.0001$) and *E* ($F_{9,27} = 61.27$, $p < 0.0001$). Unless otherwise stated, all data above comes from at least $n = 3$ experiments. *ns*, non-significant.

pathogenesis of the disease remain, in most cases, largely unexplored. Here we showed that three different mutations in three distinct domains of the IP$_3$R result in decreased channel function. The extent and penetrance of disease varies with these mutations, and our data suggest that this depends on the mechanism of channel disruption and upon the pattern of inheritance. Both factors combine to alter the stoichiometry of functional subunits in the IP$_3$R tetramer and ultimately the extent of $Ca^{2+}$ release supported by the assembled channel.

Expression of each mutation in DT40-3KO cells resulted in nonfunctional IP$_3$R $Ca^{2+}$ channels, consistent with previous studies (22, 87). In each case, the complete loss in function was not due to a difference in protein localization and expression or ER store $Ca^{2+}$ content. These data indicate that it is unlikely that these mutations result in mislocalization, altered degradation, or a constitutively leaky channel pore. Instead, the altered functionality occurred by mutation specific mechanisms. Patients harboring a mutation of Arg-269 to both a larger tryptophan and smaller glycine present with early-onset, nonprogressive SCA. Our data show that the R269W mutation resulted in a severe disruption of IP$_3$ binding. Mechanistically this is consistent with the substitution of the positively charged arginine residue with the neutral tryptophan residue impeding the coordination of negatively charged phosphate moieties of IP$_3$ in the binding pocket. In addition, it is likely that the bulky rings of the tryptophan residue may also sterically hinder IP$_3$ binding to other critical residues in the binding pocket core. Both factors likely severely compromise the conformational change in the binding pocket necessary for communication of the gating information required for channel opening.

The N602D mutant, in contrast to the R269W mutant, did not alter IP$_3$ binding. These results correlate with data showing

that this region of the receptor is outside of the $IP_3$-binding core (22). This mutation, together with the T594I mutation is located between two $\alpha$-helices in the ARM1 domain, adjacent to the LBD. Although it is possible that these mutations result in the alteration of $IP_3R$ activity by channel modulators, it is more likely that these mutations result in an alteration of the native $IP_3R$ conformation, which abrogates the communication of information between the binding core and the adjacent ARM1 domain. Thus, these mutations are likely best termed "gating mutants."

Binding of $IP_3$ was also not altered by mutation of G2498S. This residue is integral to the selectivity filter in the conduction pathway of the channel pore. It is likely that the mutation from a small glycine residue to a larger serine residue results in a "dead pore." Consistent with this observation, mutation of a neighboring selectivity filter residue in $IP_3R1$, Gly-2506, to both arginine (Fig. S6), and alanine also produces a similarly nonfunctional, pore mutant (26).

In contrast to expression of the mutant constructs in DT40-3KO, stable expression the R269W and N602D mutations in HEK-3KO cells resulted in channels with varying degrees of limited functionality in terms of the ability of $G\alpha_q$-coupled agonists to elicit $Ca^{2+}$ release in a subset of cells. Increased channel activity of these mutants observed in the HEK-3KO cells could be due in part to increased $IP_3R$ expression in HEK-3KO cells compared with DT40-3KO cells (Fig. S3). Conceivably, this higher expression level could facilitate receptor clustering, which would be expected to amplify small, unitary $Ca^{2+}$ signals. Additionally, it is possible that HEK cells express so-called "licensing" factors, which are reported to render refractory $IP_3R$, activatable, thus revealing a degree of functionality to mutant $IP_3R$ modulated in this fashion (63). Other factors could also contribute to increased functionality in HEK-3KOs including differences in accessory proteins, regulation, and the intracellular environment present in avian *versus* mammalian cells. In contrast to R269W and N602D $rIP_3R1$, stable expression of G2498S $mIP_3R2$ or G2506R $hIP_3R1$ in HEK-3KO cells failed to yield functional channels, reflecting the severe disruption of the channel pore.

Experiments documenting the activity in both DT40-3KO and HEK-3KO of the mutants stably expressed as homotetramers provides some insight into the mechanisms underlying the altered activity. However, both the R269W and N602D are inherited in an autosomal dominant manner, as are the vast majority of documented diseases associated with $IP_3R$ mutations (Tables S2–S4). Given that $IP_3Rs$ are well documented to form heterotetramers and this is the dominant $IP_3R$ form when multiple species are expressed (64), it would be predicted that these patients express a variety of tetramers comprised of different ratios of WT $IP_3R1$ and mutant monomers. Indeed, our data confirms that heterotetramers of WT and WT channels are readily assembled. How incorporation of mutant monomers with altered activity influences the function of the assembled channel is therefore an important question. We address this issue using concatenated $IP_3R$ constructs as a powerful tool to precisely control the stoichiometry of WT *versus* mutant subunits in the tetramer.

For example, heterotetramers consisting of two WT subunits and two R269W subunits are predominantly nonfunctional. Our previous studies have indicated that because of the requirement of each monomer to be liganded by $IP_3$, binding deficient mutants effectively act as dominant-negative modulators if incorporated into the heterotetramer (57). These results are also consistent with previous work from our laboratory showing other $IP_3R1$ mutations inherited in an autosomal dominant manner that result in Gillespie syndrome are dominant-negative (65). Moreover, these results suggest that in patients with heterozygous expression of these mutant proteins, only WT homotetramers will be able to contribute a significant amount of $Ca^{2+}$ release. An extension of this idea, if it is assumed that tetramers form without bias, is that given a normal distribution of mutant and WT subunits in the tetramer, only a small percentage (~9%) would be predicted to be homotetramers of WT subunits, likely severely attenuating $Ca^{2+}$ release of the compliment of $IP_3R1$ expressed.

Tetramers assembled from dimers consisting of a WT and a N602D mutant, thus expressing two mutant and two WT subunits, respectively, were similarly largely nonfunctional. Notably, however, expression of a concatenated tetramer with three WT subunits and one mutated N602D subunit resulted in a significant increase in channel function compared with cells expressing equal numbers of mutant and WT subtypes, indicating that the N602D subunit does not function as a true "dominant-negative." Although the channel activity of this mutant tetramer is still significantly decreased compared with tetramers with four WT $IP_3R1$ subunits (WT homotetramers), these data would predict that heterozygous individuals would express a greater percentage of $IP_3R$ tetramers, which retain function when compared with individuals expressing the R269W mutation.

In contrast to the R269W and N602D mutants, anhidrosis caused by the G2498S mutation is one of the few documented $IP_3R$ disorders that is inherited in an autosomal recessive manner (55). Although individuals homozygous for the mutation exhibit a profound heat intolerance through the inability to sweat, those heterozygous for the mutation are asymptomatic. Symptomatic individuals are therefore homozygous for the expression of the mutant proteins, whereas heterozygous individuals would be predicted to express a combination of mutant and WT subunits. Our data using concatenated dimers of mutant and WT subunits provides insight into why heterozygous individuals are asymptomatic. We demonstrate that heterotetramers comprised of two WT $IP_3R2$ subunits and two G2498S mutant subunits retain a significant amount of function, such that $G\alpha_q$-coupled stimulation results in $Ca^{2+}$ release activity intermediate between that of the WT homotetramers and the G2498S mutant homotetramers. Thus, these data indicate that in individuals heterozygous for the mutation, potentially a larger fraction of $IP_3R2$ channels are functional and thus presumably provide a sufficient $Ca^{2+}$ signal to sustain sweat secretion. Notably, numerous cell types in the periphery, including hepatocytes and exocrine cells, express $IP_3R2$, usually in combination with other isoforms. These data

likely also explain the highly specific phenotype observed with this mutation; whereas human sweat glands almost exclusively express $IP_3R2$, there appeared to be no obvious consequences of expression of the mutant in other tissues likely because the G2498S mutation does not act in a dominant-negative fashion. Thus, heterotetramers of mutant and other WT $IP_3R$ subtypes would not be predicted to be substantially disabled and thus impact cellular function. In total, studies presented here using concatenated subunits provide unprecedented insight into how mutant $IP_3R$ may function in heterozygous individuals and help demystify these challenging channelopathies.

## Experimental procedures

### Reagents

Antibodies generated by Pocono Rabbit Farms and Laboratories included rabbit polyclonal antibodies for $IP_3R2$ against amino acids 320-338 (NT2) and amino acids 2686-2701 in mouse $IP_3R2$ (CT2), as well as a rabbit polyclonal antibody against the C-terminal 19 aa of $IP_3R1$ (CT1) (66). Reagents used for SDS-PAGE were obtained from Bio-Rad. Protein A/G-agarose beads were from Santa Cruz. Alexa Fluor 488 and Dylight™ 800CW secondary antibodies were from Thermo Scientific. Restriction enzymes and DNA T4 ligase were purchased from New England Biolabs. β-Mercaptoethanol, chicken serum, penicillin/streptomycin, RPMI 1640 media, and G418 sulfate were obtained from Life Technologies. Fetal bovine serum and goat serum were from Gibco. Fura2-AM was from TEFLABS. All other chemicals were obtained from Sigma unless otherwise indicated.

### Plasmid construction

Mutagenesis and all DNA modifications were carried out using *Pfu* Ultra II Hotstart 2× Master Mix (Agilent). Primers used in this study were synthesized by Integrated DNA Technologies (IDT) (Table S5). A QuikChange mutagenesis protocol was used to introduce R269W in cDNAs encoding the rat $IP_3R1$ ($rIP_3R1$; NM_001270596) in pDNA3.1 using mutagenic primers (primers 1 and 2). These primers encode R269W, in addition to silently introducing the indicated restriction site (Table S5). Similarly, two mutagenesis primers were used to introduce N602D into $rIP_3R1$ (primers 5 and 6), whereas mutagenesis primers were used to introduce R269W (primers 3 and 4), T494I (primers 7 and 8), and G2506R (primers 9 and 10 for G > A and primers 11 and 12 for G > C) into human $IP_3R1$ ($hIP_3R1$; NM_001099952) in pCDNA3.1 (obtained from Annetta Wronska at Columbia University). Finally, primers 13 and 14 introduced G2498S in mouse $IP_3R2$ ($mIP_3R2$; NM_019923) in pcDNA3.1. The coding regions for all constructs were confirmed by sequencing.

$IP_3R1$ and $IP_3R2$ concatenated constructs were generated as previously described in detail (38, 64, 67). Briefly, the cDNAs of the corresponding $IP_3R$ subunits, designated as head and tail, in pcDNA3.1 vector was modified and subcloned in a tandem fashion, between the two arms of the pJAZZ mamm linear vector (Lucigen). The resultant construct encodes one ORF consisting of two $IP_3R$ subunits connected with a 14-amino acid linker. Similarly, tetrameric $IP_3R1$ constructs were generated using four modified $IP_3R1$ subunits (numbered I-IV). The resulting cDNA forms one reading frame encoding four $IP_3R1$ subunits with 14 amino acid linkers separating the subunits. To create concatenated constructs harboring one or more mutant subunits, the corresponding mutations were introduced in the individual subunits before assembling the concatenated constructs.

### Cell culture and transfection

DT40-3KO, chicken B lymphocyte cells engineered through homologous recombination for the deletion of the three endogenous $IP_3R$ isoforms (56), were grown at 39 °C with 5% $CO_2$ in RPMI 1640 media supplemented with 1% chicken serum, 10% fetal bovine serum, 100 units/ml of penicillin, 100 μg/ml of streptomycin. DT40-3KO transfection was performed as described before (66). In brief, 5 million cells were washed once with PBS and electroporated with 5-10 μg of DNA using Amaxa cell nucleofector kit T (Lonza laboratories). Cells were allowed to recover for 24 h at 39°C with 5% $CO_2$, and then passed into 96-well–plates containing media supplemented with 2 mg/ml of G418. Clones expressing the desired constructs were identified by immunoblots 10-14 days after transfection. HEK-3KO, HEK293 cells engineered in our laboratory though CRISPR/Cas9 for the deletion of the three endogenous $IP_3R$ isoforms were grown at 37 °C with 5% $CO_2$ in Dulbecco's modified Eagle's medium supplemented with 10% fetal bovine serum, 100 units/ml of penicillin, 100 μg/ml of streptomycin.

HEK-3KO transfection was also performed similarly to as previously described (57). In brief, 1 million cells were washed once with PBS and electroporated with 5-10 μg of DNA using Amaxa cell nucleofector kit T (Lonza laboratories). Cells recovered for 48 h at 37 °C with 5% $CO_2$, and then were passed into new 10-cm plates containing media supplemented with 2 mg/ml of G418. After 7 days of selection, immunoblot was performed to assess expression of the desired constructs in these stable HEK cell pools. Following confirmation of expression, cells were either picked and transferred to new 24-well– plates or diluted at various concentrations into 96-well–plates or containing media supplemented with 2 mg/ml of G418. Monoclonal lines were identified 7 days after dilution and clones expressing the desired constructs were identified by immunoblots 10-14 days after identification.

### Cell lysis, co-immunoprecipitation, and SDS-PAGE analyses

Following treatment, cells were harvested by centrifugation, washed once with PBS, and solubilized in cell lysis buffer containing 10 mm Tris-HCl, 10 mM NaCl, 1 mM EGTA, 1 mM EDTA, 1 mM NaF, 20 mM $Na_4P_2O_7$, 2 mM $Na_3VO_4$, 1% Triton X-100 (v/v), 0.5% sodium deoxycholate (w/v), and 10% glycerol supplemented with protease inhibitors. Lysates were incubated for 30 min on ice and cleared by centrifugation at 16,000 × *g* for 10 min at 4 °C. Protein concentrations in cleared lysates were determined using Dc protein assay kit (Bio-Rad). Cleared supernatants were rocked with the indicated antibodies and 30 μl of protein A/G slurry overnight. Immunocomplexes were washed five times and resuspended in gel loading buffer.

Proteins were fractionated on SDS-PAGE gel and transferred to a nitrocellulose membrane, which was probed with the indicated primary antibodies and corresponding secondary antibodies. Membranes were imaged with an Odyssey IR imaging system (LICOR Biosciences).

### Immunocytochemistry and confocal microscopy

Stable HEK cell lines were plated on poly-D-lysine–coated coverslips. When roughly 50% confluent cells were fixed using ice-cold methanol at −20 °C or paraformaldehyde at room temperature for 10 min. Subsequently, coverslips were washed with PBS and cells were blocked in goat serum or BSA for 1.5 h. Following blocking, cells were incubated in primary antibody ($IP_3R1$ or $IP_3R2$) and DAPI overnight at 4 °C. The following day, primary antibody was removed, and coverslips were washed 3 times with PBS for 10 min with gentle rocking. Subsequently, the secondary antibody conjugated to Alexa Fluor 488 or 594 was incubated for 1 h at room temperature with gentle rocking. After incubation, coverslips were washed with PBS and mounted on slides. After allowing slides to dry, coverslips were sealed onto slides and imaged using confocal microscopy.

### Measurement of cytosolic $Ca^{2+}$ in intact cells

Single cell $Ca^{2+}$ imaging was performed as described previously (66). DT40-3KO and HEK-3KO cells expressing $IP_3R$ constructs were washed once with imaging buffer (10 mM HEPES, 1.26 mM $Ca^{2+}$, 137 mM NaCl, 4.7 mM KCl, 5.5 mM glucose, 1 mM $Na_2HPO_4$, 0.56 mM $MgCl_2$, pH 7.4). Cells were then resuspended in imaging buffer containing 2 $\mu$M Fura2-AM and placed on a coverslip for 20 min at room temperature to allow for fluorescent dye loading and attachment of cells to the glass coverslip. Cells were then perfused with imaging buffer and stimulated with the desired agonist. $Ca^{2+}$ imaging was performed using an inverted epifluorescence Nikon microscope with a ×40 oil immersion objective. Cells were alternately excited at 340 and 380 nm, and emission was monitored at 505 nm. Images were captured every second with an exposure of 10 ms and 4 × 4 binning using a digital camera driven by TILL Photonics software. Image acquisition was performed using TILLvisION software and data were exported to Microsoft excel. Experiments were repeated at least three times.

Population-based $Ca^{2+}$ imaging was performed in intact HEK cells by loading cells with 4 $\mu$M Fura-2 AM in culture medium. After 1 h, cells were harvested and subsequently washed, resuspended in imaging buffer, and dispensed into a black-walled flat-bottom 96-well–plate (~300,000 cells/well). The plate was spun at 200 × *g* for 2 min to plate cells to the bottom of each well. The plate rested for 30 min prior to commencing the assay. Fluorescence imaging was carried out using FlexStation 3 from Molecular Devices (excitation alternated between 340 and 380 nm and emission 510 nm) and analyzed by using SoftMax© Pro Microplate Data Acquisition and Analysis software to determine peak of the response. Data were averaged from at least 3 individual plates and curves fitting was done using a logistic dose-response equation in the OriginPro 6.1 software.

### Single cell-permeabilized DT40 cell $IP_3$-induced $Ca^{2+}$ release (IICR) assays

DT40-3KO cells stably expressing defined $IP_3R$ constructs were loaded with 20 $\mu$M MgFura-2 AM for 50–60 min and subsequently permeabilized by superfusion of 40 $\mu$M $\beta$-escin in imaging buffer as previously described (57, 64). The duration of permeabilization depended on the flow rate, and care was taken to prevent excessive (internal membrane) permeabilization by careful monitoring of the fluorescence. Permeabilized cells were then washed in ICM without $\beta$-escin for 15 min to facilitate removal of cytosolic dye. The internal stores of permeabilized cells were loaded by activating SERCA through superfusion with ICM containing 1.4 mM $MgCl_2$, 3 mM NaATP, and 0.65 mM $CaCl_2$ (free [$Ca^{2+}$] of 200 nM (MaxChelator freeware)). Upon stabilization of fluorescence, $MgCl_2$ was removed from the superfused solution to disable SERCA. Varying concentrated $IP_3$ were applied through superfusion to induce unidirectional $Ca^{2+}$ release from internals stores. After washing out $IP_3$, stores were repeatedly refilled and released to allow for repeated stimulations. Each experiment contained between 30 and 60 cells in a field of view and performed a minimum of three times. The initial rates of $Ca^{2+}$ release were determined by fitting the release curves of each individual cell to a single exponential function (OriginPro 6.1). Concentration-response curves were plotted using the determined rates. All imaging was performed on an inverted epifluorescence Nikon microscope with a ×40 oil immersion objective. Cells were alternately excited at 340 and 380 nm, and emission was monitored at 505 nm. Images were captured every 5 s during permeabilization, loading, and disabling and every second during release. This was done with an exposure of 10 ms and 4 × 4 binning using a digital camera driven by TILL Photonics software.

### Competitive $IP_3$-binding assay

DT40-3KO cells stably expressing the indicated $IP_3R$ constructs were washed once with PBS and lysed in Igepal lysis buffer containing (120 mM NaCl, 50 mM Tris-HCl, 0.5% Igepal (v/v), 1 mM EDTA) supplemented with a mixture of protease inhibitors. Lysates were incubated on ice for 30 min and cleared by centrifugation at 16,000 × *g* for 10 min at 4 °C. $IP_3R$ proteins were immunoprecipitated overnight using anti-$IP_3R$ and protein A/G PLUS-agarose beads. Immunocomplexes were washed three times with lysis buffer and twice with binding buffer (50 mM Tris-base, 1 mM EDTA, pH 8, plus 1 mM $\beta$-mercaptoethanol) and equally distributed into 1.5-ml microcentrifuge tubes. One pair of tubes was immunoblotted using SDS-PAGE to ensure equal immunoprecipitation of WT and mutant protein, whereas all others underwent the binding reaction consisting of a 100-$\mu$l volume containing equal amounts of immunoprecipitated proteins, 2.5 nM tritiated $IP_3$ ([$^3$H]$IP_3$) in the presence of different concentrations of unlabeled $IP_3$. Tubes were incubated for 1 h at 4 °C with mixing every 10 min. Finally, tubes were centrifuged at 16,000 × *g*, supernatants were removed, and 500 µl of 1% of SDS was added to each tube. The contents of the tubes were transferred to vials containing scintillation liquid after 12 h and bound radioactivity were measured using liquid scintillation counter. Nonspecific

binding was calculated as the amount of bound radioactivity in the presence of 50 $\mu$M unlabeled $IP_3$. Specific binding is determined by subtracting nonspecific binding from the CPM values obtained in other conditions. Total specific binding was determined as the binding observed in the absence of unlabeled $IP_3$. Normalized specific binding from 3 experiments were averaged and curves were fit using a logistic dose-response equation using the OriginPro 6.1 software.

### *Data analysis and statistical analysis*

Data obtained were exported into Microsoft Excel where appropriate ratios, normalizations, and averages were calculated. Statistical analysis was performed in GraphPad Prism for experiments comparing two cell lines (unpaired *t* test) and three or more cell lines (one-way ANOVA with Tukey's test). Logistic fits, as well as $IC_{50}$ were calculated using OriginPro 6.1.

## Data availability

All constructs used are available freely on request. All data needed to evaluate the conclusions are presented in the paper or Supporting material.

*Acknowledgments*—The thank Dr. Irina Serysheva and Dr. Mariah Baker (University of Texas, Health Science Center at Houston) for helpful insights into the structural consequences of these missense mutations. We also thank members of the lab, especially Sydney Stremick for helpful and constructive comments.

*Author contributions*—L. E. T. formal analysis; L. E. T., K. J. A., A. M. W., and S. M. investigation; L. E. T. writing-original draft; K. J. A. and D. I. Y. conceptualization; K. J. A. and A. M. W. methodology; SM and D. I. Y. data curation; D. I. Y. funding acquisition; D. I. Y. project administration; D. I. Y. writing-review and editing.

*Funding and additional information*—This work was supported by National Institutes of Health Grant R01 DE014756 (to D. I. Y.). The content is solely the responsibility of the authors and does not necessarily represent the official views of the National Institutes of Health.

*Conflict of interest*—The authors declare no conflicts of interest in regards to the content of this manuscript.

*Abbreviations*—The abbreviations used are: $IP_3$, inositol 1,4,5-trisphosphate; $IP_3R$, inositol 1,4,5-trisphosphate receptor; LBD, ligand-binding domain; SCA, spinocerebellar ataxia; aa, amino acid (s); GS, Gillespie syndrome; PAR, protease-activated receptor; HEK, human embryonic kidney; SERCA, sarcoplasmic reticulum $Ca^{2+}$-ATPase; DAPI, 4′,6-diamidino-2-phenylindole; PDB, Protein Data Bank; ANOVA, analysis of variance; GAPDH, glyceraldehyde-3-phosphate dehydrogenase.

## References

1. Chin, K. V., Cade, C., Brostrom, C. O., Galuska, E. M., and Brostrom, M. A. (1987) Calcium-dependent regulation of protein synthesis at translational initiation in eukaryotic cells. *J. Biol. Chem.* **262,** 16509–16514 Medline
2. Nicotera, P., and Orrenius, S. (1992) $Ca^{2+}$ and cell death. *Ann. N. Y. Acad. Sci.* **648,** 17–27 CrossRef Medline
3. Berridge, M. J. (1993) Inositol trisphosphate and calcium signalling. *Nature* **361,** 315–325 CrossRef Medline
4. Berridge, M. J., Bootman, M. D., and Lipp, P. (1998) Calcium: a life and death signal. *Nature* **395,** 645–648 CrossRef Medline
5. Berridge, M. J., Lipp, P., and Bootman, M. D. (2000) The versatility and universality of calcium signalling. *Nat. Rev. Mol. Cell Biol.* **1,** 11–21 CrossRef Medline
6. Mattson, M. P., and Chan, S. L. (2003) Calcium orchestrates apoptosis. *Nat. Cell Biol.* **5,** 1041–1043 CrossRef Medline
7. Limbäck-Stokin, K., Korzus, E., Nagaoka-Yasuda, R., and Mayford, M. (2004) Nuclear calcium/calmodulin regulates memory consolidation. *J. Neurosci.* **24,** 10858–10867 CrossRef Medline
8. Harr, M. W., and Distelhorst, C. W. (2010) Apoptosis and autophagy: decoding calcium signals that mediate life or death. *Cold Spring Harbor Perspect. Biol.* **2,** a005579 CrossRef Medline
9. Iino, M. (2010) Spatiotemporal dynamics of $Ca^{2+}$ signaling and its physiological roles. *Proc. Jpn. Acad. Ser. B Phys. Biol. Sci.* **86,** 244–256 CrossRef Medline
10. Decuypere, J. P., Monaco, G., Bultynck, G., Missiaen, L., De Smedt, H., and Parys, J. B. (2011) The IP(3) receptor-mitochondria connection in apoptosis and autophagy. *Biochim. Biophys. Acta* **1813,** 1003–1013 CrossRef Medline
11. Goonasekera, S. A., and Molkentin, J. D. (2012) Unraveling the secrets of a double life: contractile versus signaling $Ca^{2+}$ in a cardiac myocyte. *J. Mol. Cell. Cardiol.* **52,** 317–322 CrossRef Medline
12. Mignery, G. A., Südhof, T. C., Takei, K., and De Camilli, P. (1989) Putative receptor for inositol 1,4,5-trisphosphate similar to ryanodine receptor. *Nature* **342,** 192–195 CrossRef Medline
13. Joseph, S. K., Lin, C., Pierson, S., Thomas, A. P., and Maranto, A. R. (1995) Heteroligomers of type-I and type-III inositol trisphosphate receptors in WB rat liver epithelial cells. *J. Biol. Chem.* **270,** 23310–23316 CrossRef Medline
14. Joseph, S. K., Boehning, D., Pierson, S., and Nicchitta, C. V. (1997) Membrane insertion, glycosylation, and oligomerization of inositol trisphosphate receptors in a cell-free translation system. *J. Biol. Chem.* **272,** 1579–1588 CrossRef Medline
15. Patel, S., Joseph, S. K., and Thomas, A. P. (1999) Molecular properties of inositol 1,4,5-trisphosphate receptors. *Cell Calcium* **25,** 247–264 CrossRef Medline
16. Onoue, H., Tanaka, H., Tanaka, K., Doira, N., and Ito, Y. (2000) Heterooligomer of type 1 and type 2 inositol 1,4,5-trisphosphate receptor expressed in rat liver membrane fraction exists as tetrameric complex. *Biochem. Biophys. Res. Commun.* **267,** 928–933 CrossRef Medline
17. Joseph, S. K., Bokkala, S., Boehning, D., and Zeigler, S. (2000) Factors determining the composition of inositol trisphosphate receptor heterooligomers expressed in COS cells. *J. Biol. Chem.* **275,** 16084–16090 CrossRef Medline
18. Foskett, J. K., White, C., Cheung, K. H., and Mak, D. O. (2007) Inositol trisphosphate receptor $Ca^{2+}$ release channels. *Physiol. Rev.* **87,** 593–658 CrossRef Medline
19. Streb, H., Irvine, R. F., Berridge, M. J., and Schulz, I. (1983) Release of $Ca^{2+}$ from a nonmitochondrial intracellular store in pancreatic acinar cells by inositol-1,4,5-trisphosphate. *Nature* **306,** 67–69 CrossRef Medline
20. Streb, H., Bayerdörffer, E., Haase, W., Irvine, R. F., and Schulz, I. (1984) Effect of inositol-1,4,5-trisphosphate on isolated subcellular fractions of rat pancreas. *J. Membr. Biol.* **81,** 241–253 CrossRef Medline
21. Iwai, M., Michikawa, T., Bosanac, I., Ikura, M., and Mikoshiba, K. (2007) Molecular basis of the isoform-specific ligand-binding affinity of inositol 1,4,5-trisphosphate receptors. *J. Biol. Chem.* **282,** 12755–12764 CrossRef Medline
22. Yoshikawa, F., Morita, M., Monkawa, T., Michikawa, T., Furuichi, T., and Mikoshiba, K. (1996) Mutational analysis of the ligand binding site of the inositol 1,4,5-trisphosphate receptor. *J. Biol. Chem.* **271,** 18277–18284 CrossRef Medline

23. Yule, D. I., Betzenhauser, M. J., and Joseph, S. K. (2010) Linking structure to function: Recent lessons from inositol 1,4,5-trisphosphate receptor mutagenesis. *Cell Calcium* **47,** 469–479 CrossRef Medline
24. Ramos-Franco, J., Galvan, D., Mignery, G. A., and Fill, M. (1999) Location of the permeation pathway in the recombinant type 1 inositol 1,4,5-trisphosphate receptor. *J. Gen. Physiol.* **114,** 243–250 CrossRef Medline
25. Boehning, D., Mak, D. O., Foskett, J. K., and Joseph, S. K. (2001) Molecular determinants of ion permeation and selectivity in inositol 1,4,5-trisphosphate receptor $Ca^{2+}$ channels. *J. Biol. Chem.* **276,** 13509–13512 CrossRef Medline
26. Schug, Z. T., da Fonseca, P. C. A., Bhanumathy, C. D., Wagner, L., 2nd, Zhang, X., Bailey, B., Morris, E. P., Yule, D. I., and Joseph, S. K. (2008) Molecular characterization of the inositol 1,4,5-trisphosphate receptor pore-forming segment. *J. Biol. Chem.* **283,** 2939–2948 CrossRef Medline
27. Fan, G., Baker, M. L., Wang, Z., Baker, M. R., Sinyagovskiy, P. A., Chiu, W., Ludtke, S. J., and Serysheva, I. I. (2015) Gating machinery of InsP3R channels revealed by electron cryomicroscopy. *Nature* **527,** 336–341 CrossRef Medline
28. Baker, M. R., Fan, G., and Serysheva, I. I. (2017) Structure of IP3R channel: high-resolution insights from cryo-EM. *Curr. Opin. Struct. Biol.* **46,** 38–47 CrossRef Medline
29. Hamada, K., Miyatake, H., Terauchi, A., and Mikoshiba, K. (2017) IP3-mediated gating mechanism of the IP3 receptor revealed by mutagenesis and X-ray crystallography. *Proc. Natl. Acad. Sci. U.S.A.* **114,** 4661–4666 CrossRef Medline
30. Fan, G., Baker, M. R., Wang, Z., Seryshev, A. B., Ludtke, S. J., Baker, M. L., and Serysheva, I. I. (2018) Cryo-EM reveals ligand induced allostery underlying InsP3R channel gating. *Cell Res.* **28,** 1158–1170 CrossRef Medline
31. Taylor, C. W., and Tovey, S. C. (2010) IP(3) receptors: toward understanding their activation. *Cold Spring Harbor Perspect. Biol.* **2,** a004010 CrossRef Medline
32. Maranto, A. R. (1994) Primary structure, ligand binding, and localization of the human type 3 inositol 1,4,5-trisphosphate receptor expressed in intestinal epithelium. *J. Biol. Chem.* **269,** 1222–1230 Medline
33. Newton, C. L., Mignery, G. A., and Sudhof, T. C. (1994) Co-expression in vertebrate tissues and cell lines of multiple inositol 1,4,5-trisphosphate (InsP3) receptors with distinct affinities for InsP3. *J. Biol. Chem.* **269,** 28613–28619 Medline
34. De Smedt, H., Missiaen, L., Parys, J. B., Henning, R. H., Sienaert, I., Vanlingen, S., Gijsens, A., Himpens, B., and Casteels, R. (1997) Isoform diversity of the inositol trisphosphate receptor in cell types of mouse origin. *Biochem. J.* **322,** 575–583 CrossRef
35. Taylor, C. W., Genazzani, A. A., and Morris, S. A. (1999) Expression of inositol trisphosphate receptors. *Cell Calcium* **26,** 237–251 CrossRef Medline
36. Furuichi, T., Yoshikawa, S., Miyawaki, A., Wada, K., Maeda, N., and Mikoshiba, K. (1989) Primary structure and functional expression of the inositol 1,4,5-trisphosphate-binding protein P400. *Nature* **342,** 32–38 CrossRef Medline
37. Wojcikiewicz, R. J. (1995) Type I, II, and III inositol 1,4,5-trisphosphate receptors are unequally susceptible to down-regulation and are expressed in markedly different proportions in different cell types. *J. Biol. Chem.* **270,** 11678–11683 CrossRef Medline
38. Alzayady, K. J., Wagner, L. E., 2nd, Chandrasekhar, R., Monteagudo, A., Godiska, R., Tall, G. G., Joseph, S. K., and Yule, D. I. (2013) Functional inositol 1,4,5-trisphosphate receptors assembled from concatenated homo- and heteromeric subunits. *J. Biol. Chem.* **288,** 29772–29784 CrossRef Medline
39. Matsumoto, M., Nakagawa, T., Inoue, T., Nagata, E., Tanaka, K., Takano, H., Minowa, O., Kuno, J., Sakakibara, S., Yamada, M., Yoneshima, H., Miyawaki, A., Fukuuchi, Y., Furuichi, T., Okano, H., *et al.* (1996) Ataxia and epileptic seizures in mice lacking type 1 inositol 1,4,5-trisphosphate receptor. *Nature* **379,** 168–171 CrossRef Medline
40. Street, V. A., Bosma, M. M., Demas, V. P., Regan, M. R., Lin, D. D., Robinson, L. C., Agnew, W. S., and Tempel, B. L. (1997) The type 1 inositol 1,4,5-trisphosphate receptor gene is altered in the opisthotonos mouse. *J. Neurosci.* **17,** 635–645 CrossRef
41. van de Leemput, J., Chandran, J., Knight, M. A., Holtzclaw, L. A., Scholz, S., Cookson, M. R., Houlden, H., Gwinn-Hardy, K., Fung, H. C., Lin, X., Hernandez, D., Simon-Sanchez, J., Wood, N. W., Giunti, P., Rafferty, I., *et al.* (2007) Deletion at ITPR1 underlies ataxia in mice and spinocerebellar ataxia 15 in humans. *PLoS Genet.* **3,** e108 CrossRef
42. Futatsugi, A., Nakamura, T., Yamada, M. K., Ebisui, E., Nakamura, K., Uchida, K., Kitaguchi, T., Takahashi-Iwanaga, H., Noda, T., Aruga, J., and Mikoshiba, K. (2005) IP3 receptor types 2 and 3 mediate exocrine secretion underlying energy metabolism. *Science* **309,** 2232–2234 CrossRef Medline
43. Bezprozvanny, I., and Hayden, M. R. (2004) Deranged neuronal calcium signaling and Huntington disease. *Biochem. Biophys. Res. Commun.* **322,** 1310–1317 CrossRef Medline
44. Foskett, J. K. (2010) Inositol trisphosphate receptor $Ca^{2+}$ release channels in neurological diseases. *Pflugers Arch.* **460,** 481–494 CrossRef Medline
45. Bezprozvanny, I. (2011) Role of inositol 1,4,5-trisphosphate receptors in pathogenesis of Huntington's disease and spinocerebellar ataxias. *Neurochem. Res.* **36,** 1186–1197 CrossRef Medline
46. Hisatsune, C., and Mikoshiba, K. (2017) IP3 receptor mutations and brain diseases in human and rodents. *J. Neurochem.* **141,** 790–807 CrossRef Medline
47. Huang, L., Chardon, J. W., Carter, M. T., Friend, K. L., Dudding, T. E., Schwartzentruber, J., Zou, R., Schofield, P. W., Douglas, S., Bulman, D. E., and Boycott, K. M. (2012) Missense mutations in ITPR1 cause autosomal dominant congenital nonprogressive spinocerebellar ataxia. *Orphanet. J. Rare Dis.* **7,** 67 CrossRef Medline
48. Parolin Schnekenberg, R., Perkins, E. M., Miller, J. W., Davies, W. I., D'Adamo, M. C., Pessia, M., Fawcett, K. A., Sims, D., Gillard, E., Hudspith, K., Skehel, P., Williams, J., O'Regan, M., Jayawant, S., Jefferson, R., *et al.* (2015) *De novo* point mutations in patients diagnosed with ataxic cerebral palsy. *Brain* **138,** 1817–1832 CrossRef Medline
49. Sasaki, M., Ohba, C., Iai, M., Hirabayashi, S., Osaka, H., Hiraide, T., Saitsu, H., and Matsumoto, N. (2015) Sporadic infantile-onset spinocerebellar ataxia caused by missense mutations of the inositol 1,4,5-triphosphate receptor type 1 gene. *J. Neurol.* **262,** 1278–1284 CrossRef Medline
50. Barresi, S., Niceta, M., Alfieri, P., Brankovic, V., Piccini, G., Bruselles, A., Barone, M. R., Cusmai, R., Tartaglia, M., Bertini, E., and Zanni, G. (2017) Mutations in the IRBIT domain of ITPR1 are a frequent cause of autosomal dominant nonprogressive congenital ataxia. *Clin. Genet.* **91,** 86–91 CrossRef Medline
51. Das, J., Lilleker, J., Shereef, H., and Ealing, J. (2017) Missense mutation in the ITPR1 gene presenting with ataxic cerebral palsy: Description of an affected family and literature review. *Neurol. Neurochir. Pol.* **51,** 497–500 CrossRef Medline
52. Zambonin, J. L., Bellomo, A., Ben-Pazi, H., Everman, D. B., Frazer, L. M., Geraghty, M. T., Harper, A. D., Jones, J. R., Kamien, B., Kernohan, K., Koenig, M. K., Lines, M., Palmer, E. E., Richardson, R., Segel, R., *et al.* (2017) Spinocerebellar ataxia type 29 due to mutations in ITPR1: a case series and review of this emerging congenital ataxia. *Orphanet. J. Rare Dis.* **12,** 121 CrossRef Medline
53. Synofzik, M., Helbig, K. L., Harmuth, F., Deconinck, T., Tanpaiboon, P., Sun, B., Guo, W., Wang, R., Palmaer, E., Tang, S., Schaefer, G. B., Gburek-Augustat, J., Züchner, S., Krägeloh-Mann, I., Baets, J., *et al.* (2018) *De novo* ITPR1 variants are a recurrent cause of early-onset ataxia, acting via loss of channel function. *Eur. J. Hum. Genet.* **26,** 1623–1634 CrossRef
54. McEntagart, M., Williamson, K. A., Rainger, J. K., Wheeler, A., Seawright, A., De Baere, E., Verdin, H., Bergendahl, L. T., Quigley, A., Rainger, J., Dixit, A., Sarkar, A., López Laso, E., Sanchez-Carpintero, R., Barrio, J., *et al.* (2016) A restricted repertoire of *de novo* mutations in ITPR1 cause Gillespie syndrome with evidence for dominant-negative effect. *Am. J. Hum. Genet.* **98,** 981–992 CrossRef Medline
55. Klar, J., Hisatsune, C., Baig, S. M., Tariq, M., Johansson, A. C., Rasool, M., Malik, N. A., Ameur, A., Sugiura, K., Feuk, L., Mikoshiba, K., and Dahl, N. (2014) Abolished InsP3R2 function inhibits sweat secretion in both humans and mice. *J. Clin. Invest.* **124,** 4773–4780 CrossRef Medline
56. Sugawara, H., Kurosaki, M., Takata, M., and Kurosaki, T. (1997) Genetic evidence for involvement of type 1, type 2 and type 3 inositol 1,4,5-

trisphosphate receptors in signal transduction through the B-cell antigen receptor. *EMBO J.* **16,** 3078–3088 CrossRef Medline
57. Alzayady, K. J., Wang, L., Chandrasekhar, R., Wagner, L. E., 2nd, Van Petegem, F., and Yule, D. I. (2016) Defining the stoichiometry of inositol 1,4,5-trisphosphate binding required to initiate Ca2+ release. *Sci. Signal* **9,** ra35 CrossRef Medline
58. Terry, L. E., Alzayady, K. J., Furati, E., and Yule, D. I. (2018) Inositol 1,4,5-trisphosphate receptor mutations associated with human disease. *Messenger* **6,** 29–44 CrossRef
59. Kerkhofs, M., Seitaj, B., Ivanova, H., Monaco, G., Bultynck, G., and Parys, J. B. (2018) Pathophysiological consequences of isoform-specific IP3 receptor mutations. *Biochim. Biophys. Acta Mol. Cell Res.* **1865,** 1707–1717 CrossRef Medline
60. Ando, H., Mizutani, A., Matsu-Ura, T., and Mikoshiba, K. (2003) IRBIT, a novel inositol 1,4,5-trisphosphate (IP3) receptor-binding protein, is released from the IP3 receptor upon IP3 binding to the receptor. *J. Biol. Chem.* **278,** 10602–10612 CrossRef Medline
61. Ando, H., Mizutani, A., Kiefer, H., Tsuzurugi, D., Michikawa, T., and Mikoshiba, K. (2006) IRBIT suppresses IP3 receptor activity by competing with IP3 for the common binding site on the IP3 receptor. *Mol. Cell* **22,** 795–806 CrossRef Medline
62. Bosanac, I., Alattia, J. R., Mal, T. K., Chan, J., Talarico, S., Tong, F. K., Tong, K. I., Yoshikawa, F., Furuichi, T., Iwai, M., Michikawa, T., Mikoshiba, K., and Ikura, M. (2002) Structure of the inositol 1,4,5-trisphosphate receptor binding core in complex with its ligand. *Nature* **420,** 696–700 CrossRef Medline
63. Taylor, C. W., and Machaca, K. (2019) IP3 receptors and store-operated $Ca^{2+}$ entry: a license to fill. *Curr. Opin. Cell Biol.* **57,** 1–7 CrossRef Medline
64. Chandrasekhar, R., Alzayady, K. J., Wagner, L. E., 2nd, and Yule, D. I. (2016) Unique regulatory properties of heterotetrameric inositol 1,4,5-trisphosphate receptors revealed by studying concatenated receptor constructs. *J. Biol. Chem.* **291,** 4846–4860 CrossRef Medline
65. Gerber, S., Alzayady, K. J., Burglen, L., Bremond-Gignac, D., Marchesin, V., Roche, O., Rio, M., Funalot, B., Calmon, R., Durr, A., Gil-da-Silva-Lopes, V. L., Ribeiro Bittar, M. F., Orssaud, C., Héron, B., Ayoub, E., *et al.* (2016) Recessive and dominant *de novo* ITPR1 mutations cause Gillespie syndrome. *Am. J. Hum. Genet.* **98,** 971–980 CrossRef Medline
66. Alzayady, K. J., Chandrasekhar, R., and Yule, D. I. (2013) Fragmented inositol 1,4,5-trisphosphate receptors retain tetrameric architecture and form functional $Ca^{2+}$ release channels. *J. Biol. Chem.* **288,** 11122–11134 CrossRef Medline
67. Chandrasekhar, R., Alzayady, K. J., and Yule, D. I. (2015) Using concatenated subunits to investigate the functional consequences of heterotetrameric inositol 1,4,5-trisphosphate receptors. *Biochem. Soc. Trans.* **43,** 364–370 CrossRef Medline
68. Ganesamoorthy, D., Bruno, D. L., Schoumans, J., Storey, E., Delatycki, M. B., Zhu, D., Wei, M. K., Nicholson, G. A., McKinlay Gardner, R. J., and Slater, H. R. (2009) Development of a multiplex ligation-dependent probe amplification assay for diagnosis and estimation of the frequency of spinocerebellar ataxia type 15. *Clin. Chem.* **55,** 1415–1418 CrossRef Medline
69. Ohba, C., Osaka, H., Iai, M., Yamashita, S., Suzuki, Y., Aida, N., Shimozawa, N., Takamura, A., Doi, H., Tomita-Katsumoto, A., Nishiyama, K., Tsurusaki, Y., Nakashima, M., Miyake, N., Eto, Y., *et al.* (2013) Diagnostic utility of whole exome sequencing in patients showing cerebellar and/or vermis atrophy in childhood. *Neurogenetics* **14,** 225–232 CrossRef Medline
70. Fogel, B. L., Lee, H., Deignan, J. L., Strom, S. P., Kantarci, S., Wang, X., Quintero-Rivera, F., Vilain, E., Grody, W. W., Perlman, S., Geschwind, D. H., and Nelson, S. F. (2014) Exome sequencing in the clinical diagnosis of sporadic or familial cerebellar ataxia. *JAMA Neurol.* **71,** 1237–1246 CrossRef Medline
71. Wang, L., Hao, Y., Yu, P., Cao, Z., Zhang, J., Zhang, X., Chen, Y., Zhang, H., and Gu, W. (2018) Identification of a splicing mutation in ITPR1 via WES in a Chinese early-onset spinocerebellar ataxia family. *Cerebellum* **17,** 294–299 CrossRef Medline
72. Dudding, T. E., Friend, K., Schofield, P. W., Lee, S., Wilkinson, I. A., and Richards, R. I. (2004) Autosomal dominant congenital non-progressive ataxia overlaps with the SCA15 locus. *Neurology* **63,** 2288–2292 CrossRef Medline
73. Hara, K., Shiga, A., Nozaki, H., Mitsui, J., Takahashi, Y., Ishiguro, H., Yomono, H., Kurisaki, H., Goto, J., Ikeuchi, T., Tsuji, S., Nishizawa, M., and Onodera, O. (2008) Total deletion and a missense mutation of ITPR1 in Japanese SCA15 families. *Neurology* **71,** 547–551 CrossRef Medline
74. Schabhüttl, M., Wieland, T., Senderek, J., Baets, J., Timmerman, V., De Jonghe, P., Reilly, M. M., Stieglbauer, K., Laich, E., Windhager, R., Erwa, W., Trajanoski, S., Strom, T. M., and Auer-Grumbach, M. (2014) Whole-exome sequencing in patients with inherited neuropathies: outcome and challenges. *J. Neurol.* **261,** 970–982 CrossRef Medline
75. Laššuthová, P., Šafka Brožková, D., Krůtová, M., Neupauerová, J., Haberlová, J., Mazanec, R., Dřímal, P., and Seeman, P. (2016) Improving diagnosis of inherited peripheral neuropathies through gene panel analysis. *Orphanet. J. Rare Dis.* **11,** 118 CrossRef Medline
76. Shadrina, M. I., Shulskaya, M. V., Klyushnikov, S. A., Nikopensius, T., Nelis, M., Kivistik, P. A., Komar, A. A., Limborska, S. A., Illarioshkin, S. N., and Slominsky, P. A. (2016) ITPR1 gene p.Val1553Met mutation in Russian family with mild spinocerebellar ataxia. *Cerebellum Ataxias.* **3,** 2 CrossRef Medline
77. Klar, J., Ali, Z., Farooq, M., Khan, K., Wikstrom, J., Iqbal, M., Zulfiqar, S., Faryal, S., Baig, S. M., and Dahl, N. (2017) A missense variant in ITPR1 provides evidence for autosomal recessive SCA29 with asymptomatic cerebellar hypoplasia in carriers. *Eur. J. Hum. Genet.* **25,** 848–853 CrossRef Medline
78. Carvalho, D. R., Medeiros, J. E. G., Ribeiro, D. S. M., Martins, B., and Sobreira, N. L. M. (2018) Additional features of Gillespie syndrome in two Brazilian siblings with a novel ITPR1 homozygous pathogenic variant. *Eur. J. Med. Genet.* **61,** 134–138 CrossRef Medline
79. Elert-Dobkowska, E., Stepniak, I., Krysa, W., Ziora-Jakutowicz, K., Rakowicz, M., Sobanska, A., Pilch, J., Antczak-Marach, D., Zaremba, J., and Sulek, A. (2019) Next-generation sequencing study reveals the broader variant spectrum of hereditary spastic paraplegia and related phenotypes. *Neurogenetics* **20,** 27–38 CrossRef Medline
80. Gorski, M. M., Lecchi, A., Femia, E. A., La Marca, S., Cairo, A., Pappalardo, E., Lotta, L. A., Artoni, A., and Peyvandi, F. (2019) Complications of whole-exome sequencing for causal gene discovery in primary platelet secretion defects. *Haematologica* **104,** 2084–2090 CrossRef Medline
81. Stendel, C., Wagner, M., Rudolph, G., and Klopstock, T. (2019) Gillespie's syndrome with minor cerebellar involvement and no intellectual disability associated with a novel ITPR1 mutation: report of a case and literature review. *Neuropediatrics* **50,** 382–386 CrossRef Medline
82. Cetani, F., Pardi, E., Aretini, P., Saponaro, F., Borsari, S., Mazoni, L., Apicella, M., Civita, P., La Ferla, M., Caligo, M. A., Lessi, F., Mazzanti, C. M., Torregossa, L., Oppo, A., and Marcocci, C. (2020) Whole exome sequencing in familial isolated primary hyperparathyroidism. *J. Endocrinol. Invest.* **43,** 231–245 CrossRef Medline
83. Gonzaga-Jauregui, C., Harel, T., Gambin, T., Kousi, M., Griffin, L. B., Francescatto, L., Ozes, B., Karaca, E., Jhangiani, S. N., Bainbridge, M. N., Lawson, K. S., Pehlivan, D., Okamoto, Y., Withers, M., Mancias, P., *et al.* (2015) Exome sequence analysis suggests that genetic burden contributes to phenotypic variability and complex neuropathy. *Cell Rep.* **12,** 1169–1183 CrossRef Medline
84. Prasad, A., Rabionet, R., Espinet, B., Zapata, L., Puiggros, A., Melero, C., Puig, A., Sarria-Trujillo, Y., Ossowski, S., Garcia-Muret, M. P., Estrach, T., Servitje, O., Lopez-Lerma, I., Gallardo, F., Pujol, R. M., *et al.* (2016) Identification of gene mutations and fusion genes in patients with Sezary syndrome. *J. Invest. Dermatol.* **136,** 1490–1499 CrossRef Medline
85. Dentici, M. L., Barresi, S., Nardella, M., Bellacchio, E., Alfieri, P., Bruselles, A., Pantaleoni, F., Danieli, A., Iarossi, G., Cappa, M., Bertini, E., Tartaglia, M., and Zanni, G. (2017) Identification of novel and hotspot mutations in the channel domain of ITPR1 in two patients with Gillespie syndrome. *Gene* **628,** 141–145 CrossRef Medline
86. Hayashi, S., Uehara, D. T., Tanimoto, K., Mizuno, S., Chinen, Y., Fukumura, S., Takanashi, J. I., Osaka, H., Okamoto, N., and Inazawa, J. (2017) Comprehensive investigation of CASK mutations and other genetic etiologies in 41 patients with intellectual disability and microcephaly with

pontine and cerebellar hypoplasia (MICPCH). *PLoS ONE* **12,** e0181791 CrossRef Medline

87. Hsiao, C. T., Liu, Y. T., Liao, Y. C., Hsu, T. Y., Lee, Y. C., and Soong, B. W. (2017) Mutational analysis of ITPR1 in a Taiwanese cohort with cerebellar ataxias. *PLoS ONE* **12,** e0187503 CrossRef
88. van Dijk, T., Barth, P., Reneman, L., Appelhof, B., Baas, F., and Poll-The, B. T. (2017) A de novo missense mutation in the inositol 1,4,5-triphosphate receptor type 1 gene causing severe pontine and cerebellar hypoplasia: expanding the phenotype of ITPR1-related spinocerebellar ataxia's. *Am. J. Med. Genet. A* **173,** 207–212 CrossRef Medline
89. De Silva, D., Williamson, K. A., Dayasiri, K. C., Suraweera, N., Quinters, V., Abeysekara, H., Wanigasinghe, J., De Silva, D., and De Silva, H. (2018) Gillespie syndrome in a South Asian child: a case report with confirmation of a heterozygous mutation of the ITPR1 gene and review of the clinical and molecular features. *BMC Pediatr.* **18,** 308 CrossRef Medline